PIV-based pressure measurement

van Oudheusden, BW

TOPICAL REVIEW

PIV-based pressure measurement

B W van Oudheusden

Department of Aerospace Engineering, Delft University of Technology, Delft 2629 HS, The Netherlands

E-mail: b.w.vanoudheusden@tudelft.nl

Abstract
The topic of this paper is a review of the approach to extract pressure fields from flow velocity field data, typically obtained with Particle Image Velocmetry (PIV), by combining the experimental data with the governing equations. Although the basic working principles on which this procedure relies have been known for quite some time, the recent expansion of PIV capabilities have greatly increased its practical potential, up to the extent that nowadays a time-resolved volumetric pressure determination has become feasible. This has led to a novel diagnostic methodology for determining the instantaneous flow field pressure in a nonintrusive way, which is rapidly finding acceptance in an increasing variety of application areas.
The current review describes the operating principles, illustrating how the flow governing equations, in particular the equation of momentum, are employed to compute the pressure from the material acceleration of the flow. Accuracy aspects are discussed in relation to the most dominating experimental influences, notably the accuracy of the velocity source data, the temporal and spatial resolution and the method invoked to estimate the material derivative. In view of its nature of an emerging technique, recently published dedicated validation studies will be given specific attention. Different application areas are addressed, including turbulent flows, aeroacoustics, unsteady wing aerodynamics and other aeronautical applications.

Keywords: particle image velocimetry, pressure determination, material acceleration, particle tracking, particle trajectory reconstruction, turbulence, aeroacoustics, aerodynamic loads

1. Introduction

Particle Image Velocimetry (PIV) has rapidly emerged as a reliable and versatile technique for flow field measurement, capable of delivering a detailed experimental characterization of the flow in terms of (large) ensembles of instantaneous velocity fields, in an efficient and non-intrusive manner (Adrian 2005, Raffel et al. 2007, Adrian and Westerweel 2011). These velocity data and derived kinematic properties, notably vorticity, have played an important role in the experimental investigation of unsteady flows and turbulence, and their further interpretation provides essential information to increase the understanding of its governing flow physics. PIV measurement capabilities have significantly expanded by recent efforts, developing it towards a time-resolved three-dimensional technique, made possible by advances in PIV hardware (fast CMOS cameras and powerful diode-pumped lasers), improved image processing algorithms, novel PIV procedures (such as tomographic PIV, Elsinga et al. 2006, Scarano 2013), and the supporting computer infrastructure allowing for fast data acquisition, storage and processing. Thus, to date PIV has become the major diagnostic technique to accurately characterize the kinematic aspects of fluid flows.

Additional to its kinematic characteristics, fluid flow possesses a dynamic aspect that is typically represented by the fluid-dynamic pressure. The fluctuating pressure is a primary actor in turbulence, as well as in cavitation and aeroacoustic phenomena. Also, the pressure has a prominent role in determining the surface loading of objects, either steady or unsteady, with important relevance to a wide variety of engineering fields. Traditionally, the surface pressure is experimentally obtained by means of pressure orifices in the model, connected to fast responding pressure transducers or microphones in case the fluctuating surface pressure needs to be determined. More recently the optical pressure-sensitive technique Pressure Sensitive Paint (PSP) has been developed, which relies on the application of a pressure sensitive luminescent coating (McLachlan et al. 1993, Klein et al., 2005).

The instantaneous static pressure in the flow field, on the other hand, is notoriously more difficult to capture than the surface pressure. Flow pressure probes of the multiple-hole pitot-type are usually limited to provide a characterization of the mean flow field only, in view of their restricted time response capabilities as well as the point-wise measurement procedure. This, in combination with their intrusive nature, limits their applicability for the study of dynamic fluid phenomena (cf. Elliot 1972, Tsuji et al. 2007). The use of microscopic air bubbles as static pressure sensors in liquid flows has been proposed and applied by a number of investigators (Ooi and Acosta 1984, Ran and Katz 1993). The principle of operation for this technique is that the bubbles react to the ambient static pressure by a change in size, which is determined by a holographic technique. However, apart from their limited applicability range, the bubble markers provide only scarce data points, while also the pressure is not obtained simultaneously with the velocity measurement. More recently, the use of PSP coated particles has been proposed for pressure or simultaneous velocity and pressure measurement (Abe et al. 2004, Kimura et al. 2006, 2010).

Notwithstanding the ambition of these particular techniques for directly measuring the flow static pressure, none of them appear to provide the potential for field pressure determination that can match the state of the art of the current velocity measurement of PIV. This makes it understandable that several investigators have proposed and implemented methods in which the pressure is derived from the high-quality and high-resolution velocity data delivered by PIV. The basic mechanism allowing these approaches rests on combining the experimental PIV velocity data with the flow governing equations, as will be outlined in more detail in section 2. Especially the potential of performing time-resolved velocity measurements in volumetric flow domains has opened the perspective for determining the fluctuating pressure in unsteady, three-dimensional flows.

In a similar context, the forces which an object experiences when it is immersed in a fluid flow can be determined from the reaction on the flow itself through the application of control-volume principles (which represent the governing equations in integral form). This means that these forces can be

gathered from flow field information, instead of resolving the direct interaction between the fluid and the object at the object surface itself. Specific well-known implementations of this principle are the wake-traverse method to determine the drag of an airfoil or the wake plane study for aircraft configuration analysis. Also in this area the non-intrusive, velocimetry-based methods have been introduced (Unal et al. 1997). The pressure information may be a required ingredient in this context, although alternative approaches exist that allow forces to be determined completely from kinematic flow characteristics (velocity and vorticity) without the explicit need for the pressure (Noca et al. 1999). The further discussion of the details and implementations of PIV-based loads determination techniques is, however, outside the scope of the current overview, which puts its particular focus on the PIV-based determination of the pressure field.

Although the use of fundamental concepts that relate pressure and loads to kinematic flow field information (velocity and vorticity) have already a long standing history in aerodynamics practice in different forms of application, these have traditionally been based on flow field information gathered by a sequential scanning of the flow domain of interest by means of pressure probes. The additional capabilities of PIV would appear in this respect to make it an interesting alternative technique to provide similar information in a different way.

Also from a historical perspective, it may be illustrative to view a PIV-based pressure and loads determination as a change of paradigm versus the traditional pressure-probe based flow field analysis, while still relying on the same flow governing equations. This may be exemplified by the Bernoulli equation that applies for steady incompressible and irrotational flow:

$$p + \frac{1}{2}\rho V^2 = p_\infty + \frac{1}{2}\rho V_\infty^2 \tag{1}$$

This equation provides a link between local pressure and velocity magnitude V, that may be employed on the one hand to infer velocity from pressure measurements (the basis of the pitot probe) but also it would allow for the pressure determination from velocity information that can be exploited in the PIV-based pressure determination approach, provided the assumed flow conditions apply. Evidently, the situation in realistic measurement conditions will seldom be so simple that the above Bernoulli-based approach is sufficient for determining the pressure in the flow directly from the PIV data, and more elaborate procedures need to be called upon.

The specific purpose of the present review is to expose different approaches that have been reported to obtain the flow-field pressure, with notably the planar capability of PIV in mind. We will consider the underlying theoretical framework, review a number of specific validation studies as well as present a selection of applications.

As a final comment, it is remarked here that notwithstanding the particular focus put here on methods to extract pressure and loads from PIV data, this is not meant to imply that these approaches are necessarily proposed as the most preferred procedure to obtain these properties under all conditions. Industrial wind tunnel practice relies strongly on established techniques to measure surface pressures and integral aerodynamic loads by means of pressure systems and mechanical balances that have an accuracy and productivity that may be quite superior to suggested PIV equivalents. However, in other conditions the PIV-based approach may provide an attractive or even the only feasible approach, for example when dealing with situations when model instrumentation is problematic or even impossible: icing on airfoils (De Gregorio 2006) or the observations of freely flying birds or insects for example (Spedding and Hedenström 2009). Also in the study of fluid-structure interactions, which may involve highly unsteady flow phenomena in combination with pronounced deformations of the solid surfaces, the possibility to relate the loads to the flow field information provides an appealing approach of analysis. It would permit to interpret how the flow unsteady behaviour is responsible for the fluctuating loads, information that may not be easily obtained otherwise, say, with different techniques used for flow field information and for load measurement, respectively.

2.   Pressure fields from velocimetry data

As stated in the introduction, our primary interest in this review lies in the derivation of pressure fields from the PIV velocity data, with a particular attention for the potential to deliver instantaneous pressure fields in unsteady flows. In the present overview context it is interesting to mention that the principle of visualization-based pressure determination has actually quite a long history, with for example the work of Schwabe (1935) predating the era of digital image processing by about half a century. Evidently, without the availability of digital image and data processing capabilities, this involved at that time a painstaking manual effort, which limited the extent to which the procedures could be put into practice, but the essential motivation is already clearly stated in this early work:

> *"When aiming for the quantitative measurement of the temporal evolution of turbulent flows, pressure measurements often pose insurmountable difficulties, as the velocities and therefore the pressures are mostly much too small to be measured. Moreover, the measurement of very small pressures requires much time, which more or less excludes the characterization of the development of time-varying (unsteady) phenomena. To circumvent these difficulties, I have on the instigation of Prof. Prandtl developed a procedure, in which the pressure distribution is completely derived from the photographic flow pattern."* [1]

Schwabe (1935) employed a cinematographic recording of particle tracers suspended in the water flow around a circular cylinder. The instantaneous velocity distribution was determined from the length of the streaklines that were formed by the tracer particles. The pressure was subsequently determined from the velocity data by means of a curvilinear grid, where the pressure was integrated along the instantaneous streamlines with the application of the unsteady Bernoulli relation, combined with the integration of the centrifugal force in the directions normal to them. The pressure at the stagnation point was taken as the reference value for the integration. Indicative results are given in Figure 1.

Abb. 5a.   Abb. 5e.

Abb. 7a.   Abb. 7b.
Abb. 7a, 7b. Linien gleichen Druckes. *a* nach Abb. 5a, *b* nach Abb. 5e.
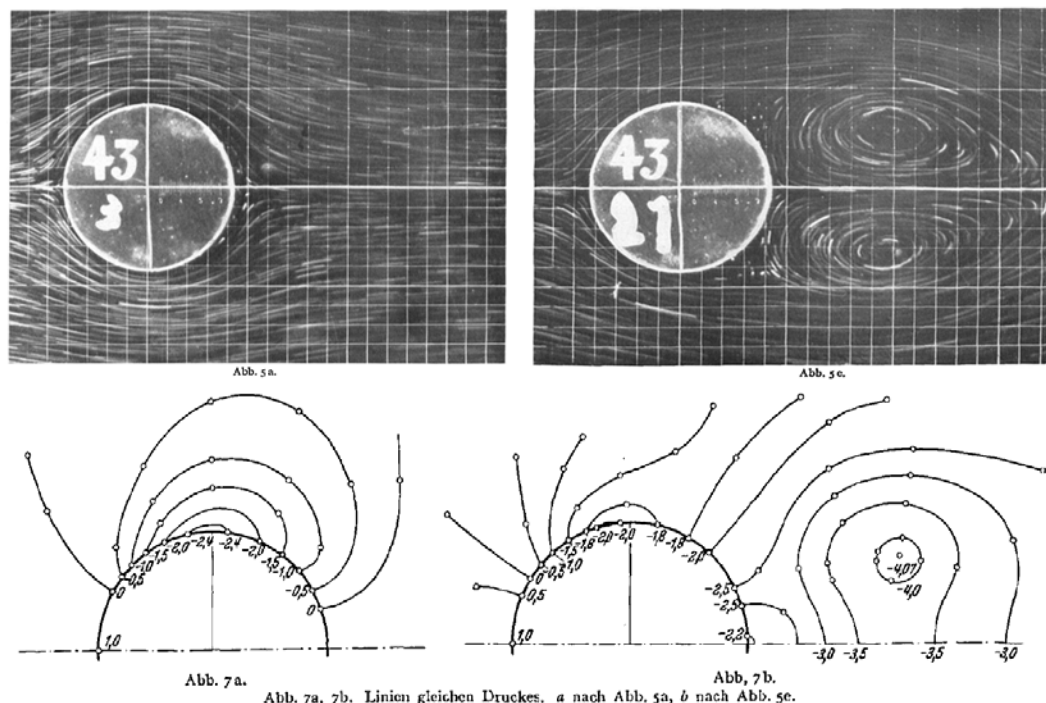
Figure 1. Flow visualizations and extracted pressure fields (isobars) for two stages in the vortex development of the flow around a circular cylinder (Schwabe, 1935). Springer

---

[1] original text in German; translation by the present author.

Much later, Imaichi and Ohmi (1983) applied a numerical processing of similar photographic flow-visualization data of two-dimensional cylinder flows. The unstructured velocity data obtained from the particle streaks was interpolated onto a regular mesh and the pressure field was subsequently obtained from a spatial integration of the pressure gradient, the latter being determined from the steady momentum equation in differential form, using finite differences. They studied the water flow around a cylinder in a towing tank. Two specific cases were considered: the formation of the wake vortex pair when the cylinder is set in motion and, secondly, the regular Karman-shedding obtained with the cylinder at constant velocity. In assessing the error estimate of the pressure determination they observed an increase of the error level, especially for the vortex-shedding case, which was attributed to "the neglect of the unsteady term" in the momentum equation.

The introduction of digital PIV (Willert and Gharib, 1991) and the associated digital data processing since then has greatly facilitated the extraction of pressure from PIV velocity data. Jakobsen et al (1997) and Jensen et al. (2001) used PIV to determine acceleration and pressure in wave phenomena. Baur and Köngeter (1999) investigated the pressure variations in vortical structures occurring in the shear layer behind a surface mounted obstacle, using a high repetition rate PIV system. A two-camera system separated by orthogonal polarization was used by Liu and Katz (2004) in order to measure the unsteady pressure in a cavity flow. More or less around the same period, steady (or time-averaged) pressure determination, for which no flow-acceleration data is required, was reported by e.g. Gurka et al. (1999) for a nozzle flow and an air jet and by Hosokawa et al. (2003) for the pressure field around bubbles in laminar flow. In more recent years, the use of PIV-based determination of pressure, either steady or unsteady, has found quite extensive application, as will be further discussed in section 3.

2.1. Theoretical background

This section provides a short outline of the general expressions to determine instantaneous pressure under unsteady flow conditions. Under incompressible flow conditions the Navier-Stokes equations can be used to compute the pressure gradient from the momentum equation, using the instantaneous velocity $\mathbf{u}$ and acceleration field and assuming the fluid density and viscosity have known values:

$$\nabla p = -\rho \frac{D\mathbf{u}}{Dt} + \mu \nabla^2 \mathbf{u} \tag{2}$$

Here $D\mathbf{u}/Dt$ is the material acceleration, i.e. the acceleration of a fluid particle followed from a Lagrangian perspective:

$$\frac{D\mathbf{u}}{Dt} = \frac{d\mathbf{u}_p(t)}{dt} = \frac{d\mathbf{u}(\mathbf{x}_p(t),t)}{dt} \tag{3}$$

where $\mathbf{x}_p(t)$ and $\mathbf{u}_p(t)$ are the position and velocity of the particle at time t, respectively. A further clarification of the material acceleration, and its practical computation, will be discussed in section 2.4. The material acceleration can also be evaluated with respect to a stationary reference frame (Eulerian perspective) as being composed of a local and convective acceleration contribution:

$$\frac{D\mathbf{u}}{Dt} = \frac{\partial \mathbf{u}}{\partial t} + (\mathbf{u} \cdot \nabla)\mathbf{u} \tag{4}$$

As an alternative approach for computing the pressure field, the Poisson equation for the pressure may be considered, which is obtained from taking the divergence of Eq.(2):

$$\nabla^2 p = \nabla \cdot (\nabla p) = \nabla \cdot (-\rho \frac{D\mathbf{u}}{Dt} + \mu \nabla^2 \mathbf{u}) \tag{5}$$

which, after substitution of Eq.(4) and under the assumption that the flow velocity field is divergence free (incompressible flow), i.e. $\nabla \cdot \mathbf{u} = 0$, reduces to:

$$\nabla^2 p = -\rho \nabla \cdot (\mathbf{u} \cdot \nabla)\mathbf{u} \tag{6}$$

Although all previous formulations (Eulerian or Lagragian, pressure-gradient or Poisson) are essentially equivalent in theory, the way in which they are implemented in practice can have an important impact on the accuracy of the resulting pressure computation. The reason for this is the different propagation of velocity error and the sensitivity to spatial and temporal discretization, associated to the use of these methods in discrete form.

In summary, the experimental determination of pressure by means of PIV can be seen to involve three steps: (1) the acquisition of velocity data with PIV; (2) the processing of the velocity data for the computation of the pressure gradient, where the material derivative is usually the dominant contribution, or alternatively the velocity-gradient terms required in the Poisson equation; and (3) the actual computation of the pressure field, by spatial integration of the pressure gradient or solution of the Poisson equation, taking appropriate boundary conditions into account. Although the first phase, that of the actual PIV measurement would appear a trivial *sine qua non,* it is important to realize that optimizing the PIV experiment for the specific purpose of pressure determination may put different or additional constraints on the PIV experiment settings.

2.2. *Planar pressure imaging in two-dimensional flow*

Although the fluid-dynamic concepts described in the previous section would in principle permit to determine the instantaneous pressure in a volumetric region of space, this would require fully 3D time-resolved experimental data, which is rarely obtainable in practice. Therefore, pressure (and force) evaluation procedures are often made to rely on planar flow characterizations, provided by 2C or 3C (stereo) PIV. Hence, in view of these planar characteristics of standard PIV procedures, pressure determination has been applied predominantly in cases where the flow is assumed to be two-dimensional, to a "sufficient" extent. The governing equations for pressure evaluation are then reduced by assuming (quasi-)2D flow, in which case the in-plane pressure gradient is obtained from the in-plane velocity and acceleration. Expansion of the momentum equation in Cartesian components then shows that under the condition of 2D incompressible unsteady flow, planar velocity and acceleration data are required to evaluate the in-plane pressure-gradient components:

$$\frac{\partial p}{\partial x} = -\rho \left\{ \frac{\partial u}{\partial t} + u \frac{\partial u}{\partial x} + v \frac{\partial u}{\partial y} \right\} + \mu \left\{ \frac{\partial^2 u}{\partial x^2} + \frac{\partial^2 u}{\partial y^2} \right\}$$

$$\frac{\partial p}{\partial y} = -\rho \left\{ \frac{\partial v}{\partial t} + u \frac{\partial v}{\partial x} + v \frac{\partial v}{\partial y} \right\} + \mu \left\{ \frac{\partial^2 v}{\partial x^2} + \frac{\partial^2 v}{\partial y^2} \right\} \tag{7}$$

Subsequent spatial integration of the instantaneous pressure gradient then delivers the planar pressure field, a procedure we may refer to as 'planar pressure imaging'. Under the same conditions, the Poisson equation for 2D flow reads:

$$\frac{\partial^2 p}{\partial x^2} + \frac{\partial^2 p}{\partial y^2} = -\rho \left\{ \left(\frac{\partial u}{\partial x} \right)^2 + 2 \frac{\partial v}{\partial x} \frac{\partial u}{\partial y} + \left(\frac{\partial v}{\partial y} \right)^2 \right\} \tag{8}$$

As noted earlier, in the Poisson formulation both the unsteady term and the viscous term have disappeared. However, this property of the Poisson formulation does not necessarily imply that it permits to infer the pressure field from instantaneous velocity fields alone, as typically time-dependent information is still needed to prescribe the boundary conditions, such as the pressure-gradient.

The above formulations show how in addition to velocity data, also acceleration data is generally needed to evaluate the instantaneous pressure field. Approaches to obtain the acceleration are either the use of a PIV system that has a sufficiently high repetition rate with respect to the flow time scales involved to permit a time-resolved flow analysis, or through the application of dual-PIV systems (Kähler and Kompenhans 2000) to produce multiple-exposures at short time separations to evaluate the acceleration, without needing a high repetition rate of the PIV (laser and camera) system itself (see e.g. Jakobsen et al. 1997, Liu and Katz 2006).

2.3. *Some consequences of applying planar PIV in a 3D flow*

Even when the planar pressure field is to be determined from the momentum equation, the contribution of out-of-plane motion needs to be accounted for in case the flow is 3D. Evidently, the question arises as to the consequence of not taking these 3D terms into account. In order to reveal the discarded terms, let the equations (2) and (3) be expanded in the (x,y)-plane of measurement, but without the restriction of 2D flow. The in-plane pressure gradient components are then given by:

$$\frac{\partial p}{\partial x} = -\rho \left\{ \frac{\partial u}{\partial t} + u\frac{\partial u}{\partial x} + v\frac{\partial u}{\partial y} \right\} + \mu \left\{ \frac{\partial^2 u}{\partial x^2} + \frac{\partial^2 u}{\partial y^2} \right\} + \left\{ -\rho w\frac{\partial u}{\partial z} + \mu\frac{\partial^2 u}{\partial z^2} \right\}$$

$$\frac{\partial p}{\partial y} = -\rho \left\{ \frac{\partial v}{\partial t} + u\frac{\partial v}{\partial x} + v\frac{\partial v}{\partial y} \right\} + \mu \left\{ \frac{\partial^2 v}{\partial x^2} + \frac{\partial^2 v}{\partial y^2} \right\} + \left\{ -\rho w\frac{\partial v}{\partial z} + \mu\frac{\partial^2 v}{\partial z^2} \right\}$$

$$(9)$$

Here, the last set of terms is related to both the out-of-plane velocity component *w* and the out-of-plane gradients of the in-plane velocity components, $\partial u/\partial z$ and $\partial v/\partial z$. This shows that for a proper in-plane pressure characterization in the presence of 3D flow motion, 2C or even 3C (stereo) PIV would not be sufficient, but additional effort is required to resolve the out-of-plane gradients, e.g. with a volumetric technique such as Tomographic PIV (Elsinga et al. 2006, Scarano 2013), or with a dual-plane approach (Kähler and Kompenhans 2000). Indeed some recent studies have been reported in which a "thin-volume" tomographic PIV approach was adopted, where the PIV measurement "plane" was extended over a small extent in the out-of-plane direction, in order to capture the required 3D information to determine correctly the instantaneous planar pressure distribution over a cross-section of the flow (Kat et al. 2009, Violato et al. 2011, Koschatzky et al. 2012).

Bauer and Köngeter (1999) proposed an approximate correction for the missing 3D information, by using the in-plane continuity equation, while Haigermoser (2009) justified his planar approach by suggesting that the calculation of the material derivative is not affected by the out-of-plane terms. However, for both arguments we can verify easily that they are, at least mathematically, equivalent to the approach where the 3D terms in equation (9) would have been neglected altogether.

In relation to the Poisson approach, its planar implementation uses the in-plane divergence component of the pressure gradient, which can be expanded as follows (Kat et al. 2008):

$$\frac{\partial^2 p}{\partial x^2} + \frac{\partial^2 p}{\partial y^2} = -\rho \left\{ \left(\frac{\partial u}{\partial x}\right)^2 + 2\frac{\partial v}{\partial x}\frac{\partial u}{\partial y} + \left(\frac{\partial v}{\partial y}\right)^2 \right\}$$

$$-\rho \left\{ \frac{\partial div_{xy}}{\partial t} + u\frac{\partial div_{xy}}{\partial x} + v\frac{\partial div_{xy}}{\partial y} \right\} + \mu \left\{ \frac{\partial^2 div_{xy}}{\partial x^2} + \frac{\partial^2 div_{xy}}{\partial y^2} \right\} \qquad (10)$$

$$-\rho \left\{ \frac{\partial w}{\partial x}\frac{\partial u}{\partial z} + \frac{\partial w}{\partial y}\frac{\partial v}{\partial z} + w\frac{\partial div_{xy}}{\partial z} \right\}$$

where $div_{xy} = \partial u / \partial x + \partial v / \partial y$ is the "in-plane divergence" of the flow field. The first set of terms describes the Poisson equation obtained under the strict assumption of 2D flow, see equation (8). The second set of terms is related to the in-plane divergence, which is neglected under the 2D assumption, but which can be evaluated from the planar PIV velocity data. Finally, the third set of terms contains the out-of-plane gradients, again not accessible to planar PIV and for which a volumetric technique is needed. It may be interesting to note, that when the Poisson approach is used as a mathematical technique to solve the pressure gradient, then the second set of terms includes the time-derivative of the in-plane divergence. This means that the Poisson formulation becomes time-dependent in its interior domain, in case the in-plane flow is not divergence-free.

Thus, in conclusion, it appears that simple ad-hoc modifications to correct planar data for out-of-plane motion do not provide an essential improvement. On the other hand, as suggested from the simulations of the pressure determination for an inclined vortex, considered by both Charonko et al. (2010) and Kat and Oudheusden (2012), a small to moderate degree of out-of-plane motion does not seriously affect the pressure field determination, provided that the local error is diffused by using a global integration approach such as a Poisson or multi-directional integration. This outcome was also confirmed by the experimental comparisons between the use of planar and 3D velocity data for 2D flows that are dominated by 2D structures (Violato et al. 2011, Kat and Oudheusden 2012, Koschatzky et al. 2012).

2.4. *Determination of the material derivative*

As outlined in the previous sections the determination of the pressure distribution involves the steps of computing the pressure-gradient from the velocity data, followed by its spatial integration. An essential first element is the determination of the material acceleration, for which in the case of an unsteady flow at least three consecutive particle images or two velocity fields obtained at known time spacing are required. Before the availability of high-speed systems, or used as a possible alternative to it, different experimental solutions have been employed to overcome the temporal resolution set by the camera framing rate. Triple-exposure imaging was used by Sridhar and Katz (1995) to measure simultaneously the velocity and material acceleration. Jakobsen et al. (1997) used a specially designed four-CCD-camera arrangement to determine the acceleration field from a sequence of four images. Chang et al. (1999) used a single camera system, with a double exposure in the first image and a single exposure in the second image. Dong et al. (2001) employed a single video camera to record double-exposed images, from which the local acceleration was determined by a combination of auto- and cross-correlation of the images. Jensen et al. (2001) report on the use of a two-camera technique, each camera recording a velocity field by an image pair resulting from the exposure by laser pulses created by shuttering the continuous wave laser by means of an acousto-optic modulator. Simultaneous velocity/acceleration measurements in a turbulent two-phase pipe flow were reported by Borowsky and Wei (2006), applying a combination of autocorrelation and crosscorrelation. Colour separation was used to discriminate between the phases. Approaches with dual-time systems separated by orthogonal polarization have been described by Christensen and Adrian (2002), Liu and Katz (2006) and Perret et al. (2006).

Based on the further procedure to process the particle images to determine the material acceleration, the following approaches may be distinguished:
- direct determination of the material acceleration from the recorded particle images themselves, either by particle tracking (Virant and Dracos 1997, Voth et al 1998, La Porta et al. 2000, Ferrari and Rossi 2008, Novara and Scarano 2012) or particle-image tracing (Jakobsen et al. 1997). In this case a true physical entity as represented by a particle (or particle ensemble) is traced between subsequent images. The time separation over which the acceleration can be reliably computed is limited by the loss of correlation as the time interval increases.
- pseudo-tracing: the material acceleration is based on reconstructing trajectories of imaginary particles from velocity fields acquired sequentially in time (see for example, Jensen et al. 2003, Liu

and Katz 2006). The limitation associated to the loss of correlation for large time separation no longer applies, as the individual velocity fields can each be determined with an optimum (relatively short) time separation. In this case the accuracy is limited by the reliability with which the fluid path can be reconstructed, based on the sequential velocity fields, i.e. the extent to which it is representative of the path of a true material particle. Especially the curvature of the trajectory may be a limiting factor.

- the Eulerian approach: the computation of the required temporal and spatial velocity dervatives is directly associated to the structured velocity measurement grid, using finite differences or linear regression (for example Imaichi and Ohmi 1983, Baur and Köngeter 1999, Jensen and Petersen 2004). Where this approach is obviously attractive for its simplicity of working with the structured data format common to the PIV method, the demands on the temporal resolution are generally more restrictive than for the tracing approach, especially for convection dominated phenomena, where the Eulerian time scale is much smaller than the Lagarangian (inherent) time scale of the flow. An approach to improve the Eulerian compuation for convective flows using Taylor's hypothesis has recently been proposed by Kat and Ganapathisubramani (2012).

In all the above approaches the determination of the velocity (or acceleration) is obtained from the correlation of particle images and forms a pre-step for obtaining the pressure using the flow governing equations. As an alternative to this segregated, sequential approach, some studies have proposed procedures in which the pressure determination is more closely integrated with the velocity determination or even the image interrogation itself, as will be discussed in section 3.

2.5. *Accuracy analysis*

The accuracy and error accumulation involved in these data processing steps contribute to the final accuracy of the pressure computation. The dominant factors of influence are here the accuracy of the underlying velocity data (PIV errors), the spatial and temporal resolution and the effect of the pressure-gradient integration procedure. It is generally accepted that for a well-designed PIV experiment the uncertainty of the velocity measurement is determined by the cross-correlation precision $\varepsilon_{CC,pix}$, for which 0.1 pixels is regarded a characteristic value (Raffel et al. 2007). The corresponding velocity uncertainty then follows as:

$$\varepsilon_u \approx \frac{\varepsilon_{CC,pix}}{M_{pix}\delta t} \tag{11}$$

where M_{pix} is the digital magnification, in pixels per unit length in the physical space, and δt the time separation between the subsequent images. In addition, the finite window size *WS* and pulse separation time δt act as spatial and temporal filter scales that limit the spatial and temporal resolution of the velocity measurement. The time separation effect has been addressed in detail by Boillot and Prasad (1996) and may become an important factor to consider when it becomes of the same order as the time step Δt used for the acceleration determination.

In the following analysis an assessment is made to estimate the error on the different approaches to the acceleration, and consequently the pressure, when derived from velocity data samples that are represented on a discrete temporal-spatial grid. The discussion presented here reflects a synthesis of a combination of reference studies (Jensen and Pedersen 2004, Perret et al. 2006, Gharali and Johnson 2008, Violato et al. 2011, Kat and Oudheusden 2012). The most important sources of error in the pressure determination come from the truncation error, due to the numerical discretization applied to estimate the acceleration, and the precision error, due to the propagation of the uncertainty of the individual velocity data. In this analysis it is assumed for convenience that the temporal spacing Δt between the subsequent velocity fields and the spatial distance $\Delta x = \Delta y = h$ between the data grid points are sufficiently small with respect to the relevant flow scales, such that a Taylor series

expansion can be applied to estimate the truncation error. Also, it is assumed that the (random) error on individual velocity measurements is uncorrelated, which is a reasonable premise when the overlap factor in the image interrogation is not significantly larger than 50%. To ensure a fair mutual comparison between the different acceleration estimates, all finite-difference schemes proposed in the discussion are taken as second-order accurate and non-staggered (in time and/or space), although higher-order interpolation schemes may be used to enhance the accuracy of acceleration (and pressure) determination.

In the Eulerian description the temporal and spatial contributions to the material accelerations are computed separately, in the form of the local and convective acceleration respectively, which are subsequently added to form the total material derivative. The second-order discretization and associated truncation error for the local acceleration is obtained as:

$$\frac{\partial \mathbf{u}}{\partial t}(\mathbf{x},t) \approx \frac{\mathbf{u}(\mathbf{x},t+\Delta t)-\mathbf{u}(\mathbf{x},t-\Delta t)}{2\Delta t} + \frac{\Delta t^2}{6}\frac{\partial^3 \mathbf{u}}{\partial t^3} \tag{12}$$

while the precision error on the local acceleration caused by the propagation of the uncertainty ε_u of the individual velocity measurement for this discretization scheme is then given by:

$$\varepsilon_{\partial \mathbf{u}/\partial t}^{\ 2} \approx \frac{\varepsilon_u^{\ 2}}{2\Delta t^2} \tag{13}$$

The two above expressions illustrate how the time separation Δt has opposite effects on the truncation error and on the uncertainty (precision) error: increasing the time separation increases the truncation error, but reduces the effect of the velocity error on the acceleration determination. The latter effect will set a lower threshold on the time separation, as discussed in Violato et al. (2011) in relation to the material acceleration, whereas in the present context the acceptable error on the acceleration due to truncation sets an upper bound. Jensen and Pedersen (2004) propose, based on the combination of truncation and precision error, an optimum time-separation estimate that would minimize the total error. For the convective acceleration, using central difference discretization in space, we obtain similarly (considering as example one particular component):

$$u\frac{\partial u}{\partial x}(x,t) \approx u(x,t)\frac{u(x+\Delta x,t)-u(x-\Delta x,t)}{2\Delta x} + \frac{\Delta x^2}{6}\frac{\partial^3 u}{\partial x^3} \tag{14}$$

while the corresponding precision error resulting from the propagation of the velocity uncertainty is:

$$\varepsilon_{u \cdot \partial u/\partial x}^{\ 2} \approx \varepsilon_u^{\ 2}\left(\frac{1}{2}\left(\frac{u}{\Delta x}\right)^2 + \left(\frac{\partial u}{\partial x}\right)^2\right) \tag{15}$$

This can be generalized for the complete spatial acceleration, assuming an equidistant grid with equal spacing in x and y directions, $\Delta x = \Delta y = h$, as follows (cf. Kat and Oudheusden 2012):

$$\varepsilon_{\mathbf{u} \cdot \nabla \mathbf{u}}^{\ 2} \approx \varepsilon_u^{\ 2}\left(\frac{1}{2}\frac{|\mathbf{u}|^2}{h^2} + |\nabla \mathbf{u}|^2\right) \tag{16}$$

Here again the opposite effects of spatial separation on the truncation and precision errors can be observed, similar as for the time separation in case of the local acceleration. Combining (13) and (16) leads to the following estimate of the precision error on the material acceleration using the Eulerian approach:

$$\varepsilon_{D\mathbf{u}/Dt}{}^2 \approx \varepsilon_u{}^2 \left(\frac{1}{2\Delta t^2} + \frac{1}{2}\frac{|\mathbf{u}|^2}{h^2} + \left|\nabla\mathbf{u}\right|^2 \right) \quad \text{(Eulerian)} \tag{17}$$
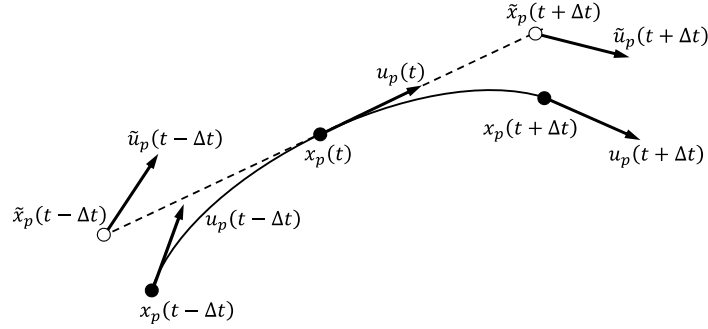

Figure 2. Illustration of the Lagrangian approach to determine the material acceleration. The solid curve represents the actual fluid trajectory, with particle positions $\mathbf{x}_p$ indicated at discrete time intervals. The dashed line represents a reconstruction of the particle path for a linear approximation, with associated estimated particle positions $\tilde{\mathbf{x}}_p$ indicated by the open circles.

The Lagrangian approach is illustrated in Figure 2. The material acceleration is obtained by computing the velocity change when following a fluid particle along its pathline, according to:

$$\frac{D\mathbf{u}}{Dt}(\mathbf{x}_p(t),t) \approx \frac{\mathbf{u}_p(t+\Delta t) - \mathbf{u}_p(t-\Delta t)}{2\Delta t} + \frac{\Delta t^2}{6}\frac{D^3\mathbf{u}}{Dt^3} \tag{18}$$

where the particle velocity $\mathbf{u}_p(t_i) = \mathbf{u}(\mathbf{x}_p(t_i),t_i)$ at a specific time instant requires the reconstruction of the particle path in order to determine the particle position $\mathbf{x}_p(t_i)$. We take here for simplicity of analysis a first-order (linear) reconstruction, to provide an estimate of the particle positions:

$$\mathbf{x}_p(t\pm\Delta t) \approx \mathbf{x}_p(t) \pm \mathbf{u}_p(t)\Delta t + \frac{\Delta t^2}{2}\frac{D^2\mathbf{u}}{Dt^2} \tag{19}$$

We see from Figure 2 that the discrepancy between the true and estimated particle positions results in a difference between the true and estimated velocities $\mathbf{u}_p$ and $\tilde{\mathbf{u}}_p$:

$$\tilde{\mathbf{u}}_p - \mathbf{u}_p \approx \left(\tilde{\mathbf{x}}_p - \mathbf{x}_p\right)\cdot\nabla\mathbf{u} \approx \frac{\Delta t^2}{2}\frac{D^2\mathbf{u}}{Dt^2}\cdot\nabla\mathbf{u} \tag{20}$$

This gives rise to an additional particle tracking error in the material derivative computation, which may be reduced by a more accurate trajectory reconstruction scheme. The uncertainty of the material acceleration computation with the Lagrangian approach is correspondingly evaluated as (Kat and Oudheusden 2012):

$$\varepsilon_{D\mathbf{u}/Dt}{}^2 \approx \varepsilon_u{}^2 \left(\frac{1}{2\Delta t^2} + \frac{1}{2}\left|\nabla\mathbf{u}\right|^2 \right) \quad \text{(Lagrangian)} \tag{21}$$

11

where the first term is caused by the propagation of the precision errors of the velocity itself, while the second term is related to the error introduced on the particle position (pathline reconstruction) as a consequence of the velocity uncertainty. It has been assumed here that the additional truncation error introduced by the interpolation of the velocity data, which is associated to the spatial resolution, can be neglected with respect to the effects of the velocity uncertainty and the temporal resolution.

2.6.   *Numerical implementation and gradient-integration strategies*

For computing the pressure from the velocity data as outlined above, the pressure gradient must be spatially integrated, imposing proper boundary conditions. Basically two strategies have been employed for this kind of problems, either a spatial-marching scheme to integrate the pressure gradient directly over the domain of investigation, or solving the Poisson equation for the pressure on that domain or a subsection of it. The two approaches appear quite different in their practical implementation, especially in view of the boundary condition treatment. The direct gradient integration can proceed from a limited area (or even a single point) where the pressure is prescribed, through a systematic spatial-marching procedure. Pressure boundary conditions may be prescribed in undisturbed flow regions or through the direct use of isentropic flow relations where appropriate. The spatial-integration procedure can be expressed as follows, where $p(\mathbf{s}_{\mathrm{ref}})$ is the pressure in the reference location:

$$p(\mathbf{s}) = p(\mathbf{s}_{\mathrm{ref}}) + \int_{\mathbf{s}_{\mathrm{ref}}}^{\mathbf{s}} \nabla p \cdot d\mathbf{s} \qquad\qquad (22)$$

The Poisson equation, on the other hand, requires boundary conditions on the entire contour of the integration domain. Typically, boundary conditions will be of mixed type: pressure prescribed where this is imposed (Dirichlet), pressure gradient over the rest of the contour (Neumann). Notwithstanding the apparent difference in the approach of the two pressure-integration strategies, spatial integration or Poisson, they are not that dissimilar from a mathematical perspective in terms of an optimization problem, as discussed by Oudheusden and Souverein (2007). For example, one may see the Poisson method as a global optimization formulation of the pressure-gradient spatial integration.

For the solution of the Poisson equation standard procedures from numerical mathematics exist, which usually follow an iterative approach, such as the SOR method applied for example by Fujisawa et al. (2005). Alternatively, spectral approaches have been suggested for solving the pressure-Poisson equation (Ragni et al. 2011a). Further details of the actual numerical implementation of a Poisson solver will not be elaborated here, as this type of formulation is encountered in many other physical problems and, hence, not specific to the pressure-determination procedure, although the aspect of the pressure boundary conditions may require specific attention, especially in the case of unsteady flow.

For the spatial-integration method different approaches have been reported; two examples are illustrated in Figure 3. Figure 3-a illustrates the structured integration procedure described by Baur and Köngeter (1999). A rectangular domain is considered and the integration starts with prescribed pressure values at one side of the domain (in this case along the top edge of the domain). The pressure field is subsequently computed by integrating row by row in the manner shown in the figure. At each integration step, all immediate neighbours in which the pressure has been determined from previous steps are used to advance the pressure solution, through a weighted value of the integration result from each individual data node. The integration procedure described in Oudheusden and Souverein (2007) was proposed as a generalized spatial-marching technique, based on a field-erosion principle, again in combination with averaged integration from neighbouring points. The technique shown in Figure 3-b was developed by Liu and Katz (2006) in the application to a rectangular observation domain corresponding to a flow cavity. The (iterative) procedure starts by establishing the pressure on the image boundary and then computing the pressure in the interior by means of a weighted omni-directional path integration procedure along lines generated from the grid points on a virtual boundary encompassing the image domain. In later implementations, a circular shape of the virtual boundary has been adopted (Haigermoser 2009, Liu and Katz 2011).
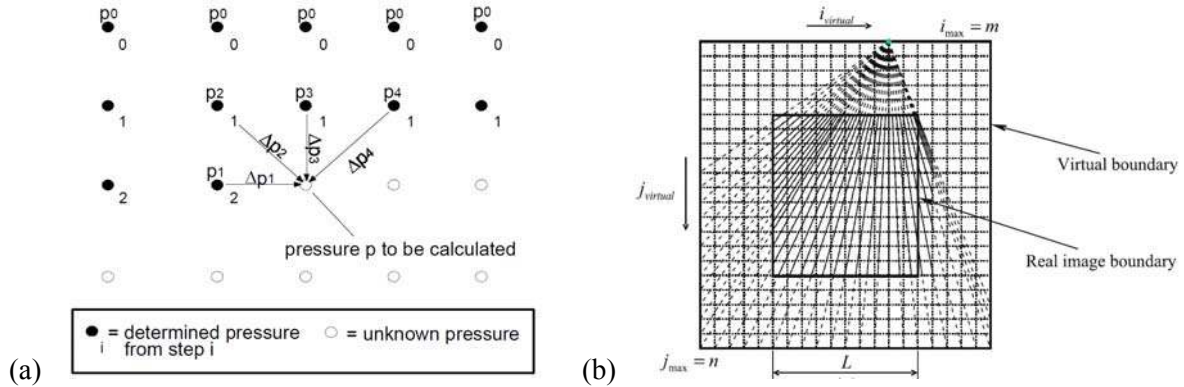
Figure 3. Spatial integration strategies: (a) space-marching integration (Baur and Köngeter,1999) ; (b) omni-directional integration (Liu and Katz, 2006)

2.7. *Comparative performance assessment studies*

A number of studies have explicitly addressed the assessment of the performance and/or comparison between different approaches of PIV-based pressure determination, based on synthetic or experimental data. Issues of particular attention have been, for example, the influence of temporal and spatial resolution of the velocity data, the propagation of error or noise in the data, and the relative performance of the difference procedures for determining the material derivative (Eulerian or Lagrangian) and for the pressure integration itself (spatial integration of the pressure gradient or a Poisson formulation). As the PIV-based method is a relatively novel approach to pressure determination, it is worthwhile to review these studies in more detail.

Different water wave phenomenon, a standing wave and a freak wave, were studied by Jakobsen et al. (1997). In their camera configuration four consecutive frames were recorded, where due to the scanning-beam illumination applied, the time separation between subsequent frames could be chosen only as an integer multiple of the scanning rate (δt =5 ms in the reported experiment). This minimum available time separation was applied between frames 1 and 2 as well as between frames 3 and 4, while a larger time separation,Δt , was applied between frames 2 and 3 in order to increase the accuracy of the acceleration measurement. To investigate the influence of the time separation, the ratio $n = \Delta t / \delta t$ was varied between 1 and 24. Eulerian and the Lagrangian procedures to obtain the material derivative were evaluated and compared, based on a simulated PIV experiment of the standing wave case. The implementation of the Eulerian method is quite straightforward: frame pairs 1-2 and 3-4 are correlated to obtain two velocity fields with a time separation of $(n+1)\delta t$, from which the acceleration is evaluated at the intermediate time (t2+t3)/2, using a finite difference formulation. For the Lagrangian method firstly frames 1 and 2 are correlated. The resulting velocity is then used as a predictor to locate the same group of particles in frame 3, after which cross-correlation of frames 2 and 3 provides a second velocity field at the intermediate time (t2+t3)/2. In this way an actual particle image tracing is carried out, i.e. the velocity and acceleration measurements are based on correlating the position of the same group of particles at different times (t1, t2 and t3). Note, however, that in this particular implementation the first velocity field is obtained from correlation over a time separation of δt , and the second one over a separation Δt , which may be substantially larger.

In the measurements of the standing wave the relative performance of the two methods was assessed in comparison to the analytical prediction of the material acceleration. Two phases of the wave were studied in more detail. The first phase is when the surface elevation passes through the still-water level, which gives minimum acceleration and maximum rate of change in acceleration. The second phase is when the surface elevation reaches its minimum value, with maximum acceleration occurring in combination with minimum time rate of change. The outcome of the assessment was that the Eulerian procedure consistently performed better than the Lagrangian approach (see Figure 4). The

latter showed larger differences with respect to the analytical prediction for small values of Δt, whereas for larger Δt it could fail completely in detecting the correct correlation of the particle group in the third image. This, according to the authors, illustrates the limitation of their Lagrangian approach "due to poor tracking or deformation of the fluid volume, with the combination of a relatively large acceleration and a long tracking time." For large values of the tracking time, the deformation of a particle group reaches such a level that the cross correlation can no longer identify the original group in the third frame. Therefore, it appears that due to the effects mentioned, the particular implementation of the Lagrangian method used in the present investigation, following a group of particle in subsequent frames, finds it limitation in the allowable time separation. This is likely to be a general conclusion for the direct particle image tracing approach. In addition, when considering the accuracy of the acceleration determination, the authors recognize the potential significant impact for the Lagrangian approach that the two velocity measurements are based on very different time intervals (δt for the first, and Δt for the second). They suggest an alternative implementation in which the correlation between frames 2 and 3 is still used to locate the original particle group in frame 3, but where the second velocity field is found from correlating images 3 and 4, but do not pursue this approach any further. Finally, the fact that the Eulerian approach performs so well can likely be attributed to the circumstance that the flow phenomenon considered is not strongly convection dominated. The convective part of the material derivative is reported to be max 10% in the standing wave study, hence, the local acceleration is dominant, which is the situation under which the approach is predicted to perform well.
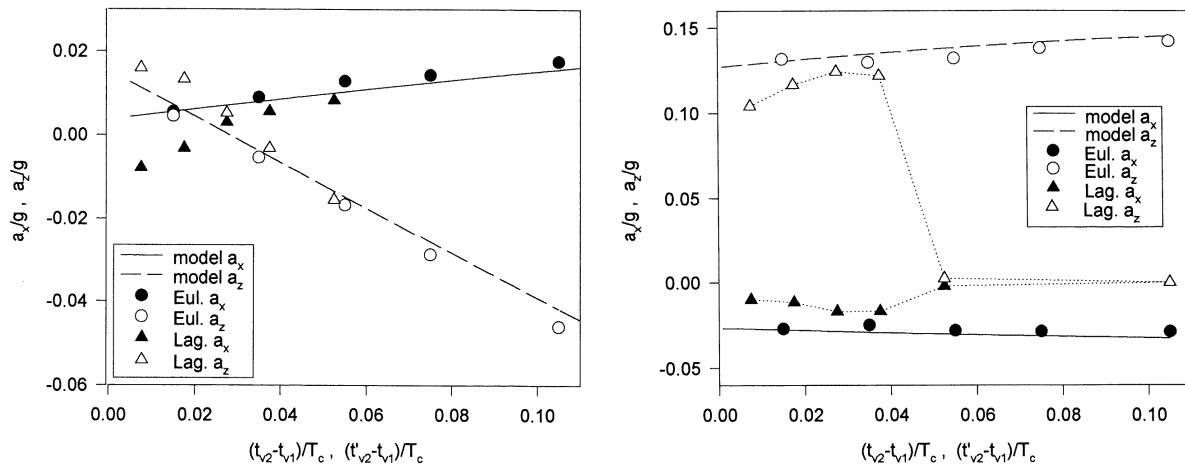

Figure 4. PIV for predictions of acceleration fields (simulated PIV method); the graphs are for the two different wave phases analysed (Jakobsen et al. 1997).

Jensen and Petersen (2004) report a similar study of acceleration measurements in wave experiments. In their Eulerian approach a linear regression (least-squares linear fit) on a neighbourhood is applied for obtaining the velocity gradient terms. Both studies report on the possibility of using spatial filtering (smoothing) or phase averaging (applicably in the case of repeatable phenomena) to reduce the effect of velocity noise.

Murai et al. (2007) report PTV measurements of the nominally 2D flow around a Savonius rotor, with the purpose to infer pressure fields and torque from the velocimetry data. The unstructured PTV data were first interpolated on a regular grid before further processing. A comparison was made between the results of using a Poisson approach or the (iterative) integration of the pressure-gradient as obtained from the Navier-Stokes equations. The pressure on the frame boundary is given by gradient-free conditions for the Navier-Stokes method, and by either uniform pressure or Neumann boundary conditions for the Poisson. Including the in-plane divergence term in the Poisson equation was found to give little difference, compare equation (10), indicating that the flow is nearly two-dimensional.

Different modifications of each method were considered. The Navier-Stokes formulation shows a higher degree of noise for the original experimental data set than the Poisson, which is removed when the velocity data are corrected to enforce two-dimensional continuity. Investigating the impact of noise in the data by adding random velocity noise vectors up to 5% of the rotor tip speed, again the Poisson equation proves to be virtually insensitive to it, due to the attenuating effect of the integration, whereas for the Navier-Stokes method the pressure noise monotonically increases with the amount of velocity noise added, see Figure 5.
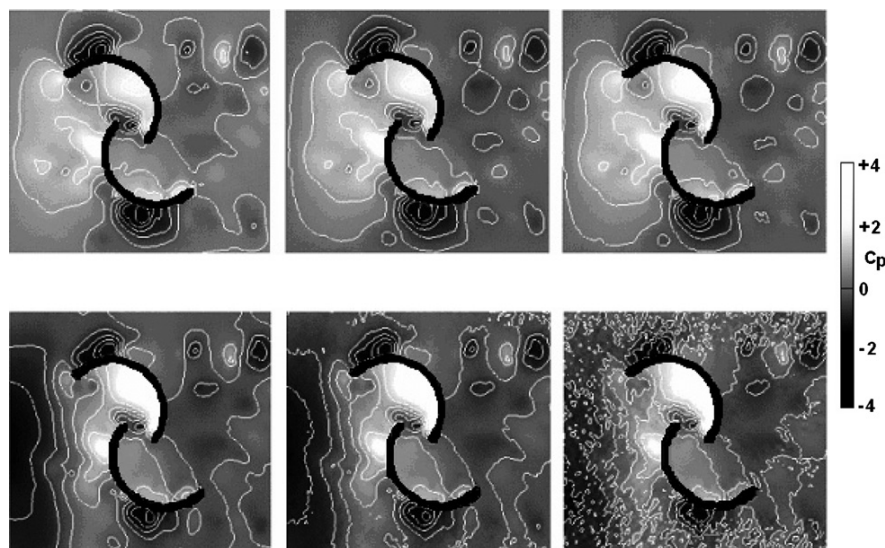

Figure 5. Pressure field estimation around a Savonius rotor from PTV data: influence of artificial velocity noise: the top row shows the results for the Poisson equation, the bottom row for the Navier–Stokes equation. Noise ratio is 0% (left), 1% (centre) or 5% for (right). The rotor is stationary in this case (Murai et al. 2007).

Charonko et al. (2010) review and compare different methods for pressure determination from PIV planar velocity fields for time-dependent incompressible flows. Several integration approaches are explored, including direct spatial integration of the pressure gradient components (multi-lines or the omni-directional approach of Liu and Katz) as well as different implementations of the Poisson equation. The computations of the velocity derivatives are performed using finite-differences on a rectangular data grid, implying that the Lagrangian approach is not considered here. Artificial data for two sample flows, a decaying vortex and a pulsatile channel flow, were used to assess the accuracy and impact of parameters such as grid resolution and sampling rate. One of the important observations reported was that error in the measured velocity fields was a significant problem for all integrations schemes. Where all schemes appear to work nearly equally well for error-free artificial velocity fields, the pressure results became "unusable" as soon as even small levels of random error were introduced. Different procedures of error reduction or data regularization were proposed as a necessary intermediate data post-processing step, such as regular low pass filtering, Lagrange minimization and POD-based smoothing. It is somewhat surprising that this issue is presented as being so crucial in this study, whereas most other investigations do not report on the need for such an extensive pre-treatment of the velocity data and appear to consider a fairly simple smoothing already sufficient to improve the pressure results, see also the study of Murai et al. (2007) discussed above. The effect of off-axis measurement and out-of-plane velocities was investigated by analysing the vortex with its axis tilted with respect to the imaging plane. It was found that all schemes that performed well for 2D viewing conditions remained to do so for misalignment angles up to about 30 degrees. As a final demonstration of the pressure determination with real PIV data, the oscillating flow in a diffuser was presented (Figure 6). The reason why different schemes responded to such a largely different extent in the study

was not clear. This led the authors to conclude that "there is no unique or optimum method for estimating the pressure field and the resulting error will depend highly on the type of the flow."
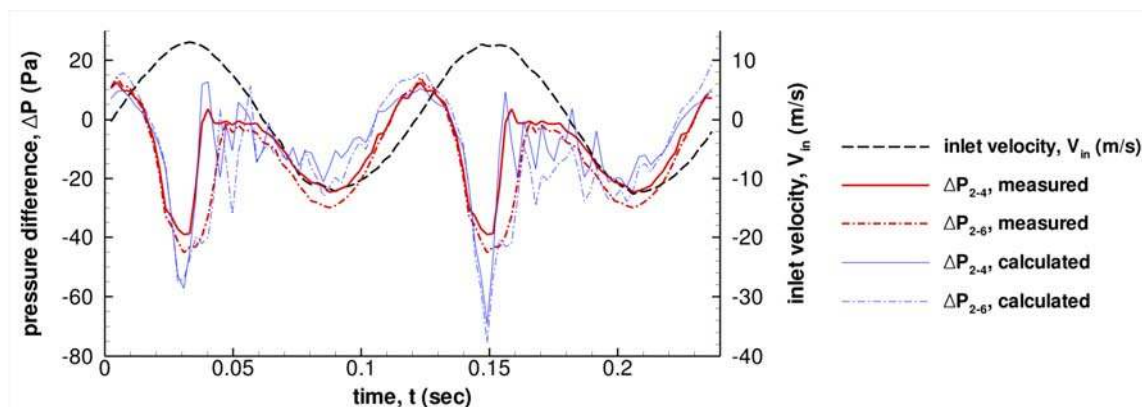

Figure 6. Charonko et al. (2010): Comparison of phase-averaged measured and calculated pressure differences between left-hand sensors 2, 4 and 6. Inlet velocity from the PIV data is plotted for reference (adapted figure kindly provided by the authors).

Violato et al. (2011) performed a comparison of Eulerian and Lagrangian pressure-determination methods in relation to the investigation of a rod-airfoil configuration, using a thin-tomo PIV technique to be able to include the out-of-plane components of the pressure gradient. Particular attention was given to the proper selection of the time separation, Δt. They proposed a guideline for the selection of its minimum value, such that the relative precision error on the material acceleration is at most 10%. On the other hand, the time separation must not be longer than a maximum value, to limit the effect of out-of-plane motion. In addition, for the Eulerian approach the time separation is limited by the time scale required for a proper sampling of the convecting flow structures. Compared with the minimum allowed time separation estimated for the Lagrangian approach, the maximum for the Eulerian approach in the wake of the cylinder (indicated by point B in Figure 7) is about two times smaller, which yields a material acceleration with a relative precision error 1.5 times larger than that estimated for the Lagrangian approach. This is reflected in the comparison between the acceleration fields depicted in Figure 7, where the results for the Eulerian approach display a higher noise level as a consequence of this. However, when looking at the resulting pressure fields obtained after integration of the material acceleration (Figure 8), the differences between Lagrangian and Eulerian methods are much less pronounced. This mitigation effect can be understood from the suppression of the error in the time-derivative term of the Euler formulation when the Poisson expression is used for the pressure integration, compare the discussion in section 2.2.

In assessment of the impact of the 3D components, a comparison was made between the 3D results and those of a 2D approach, where the Lagrangian acceleration is computed along the projected particle trajectories in the central image plane. The good correspondence between the two approaches indicates that also in this case the out-of-plane effects are small, as the measurement plane is aligned with the dominant flow direction (nearly planar flow), confirming that under these conditions a planar approach can be satisfactorily applied to determine the in-plane material acceleration and pressure field. The study also considers the case where intentionally the measurement plane is not aligned with the dominant flow direction, showing that due to the strong out-of-plane flow components, the planar approach then leads to erroneous pressure determination.
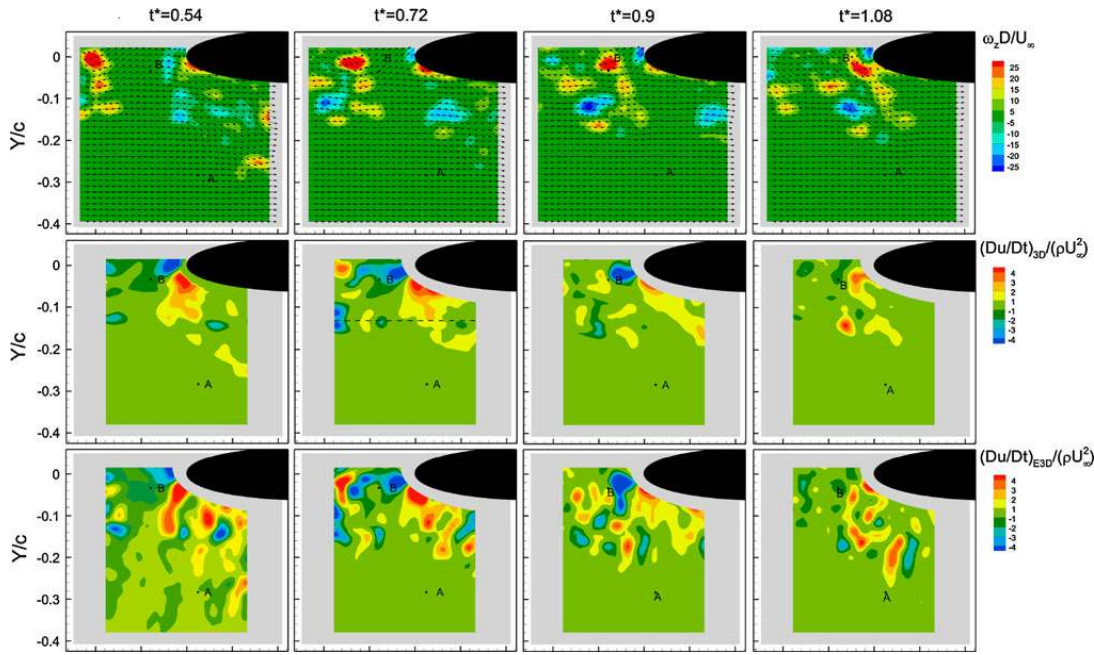
Figure 7. Rod-airfoil interaction (Violato et al. 2011); sequence of instantaneous out-of-plane vorticity contours (first row) and corresponding material acceleration according to Lagrangian method with Δt =1.2 ms (second row) and Eulerian approach with Δt =0.4 ms (third row).
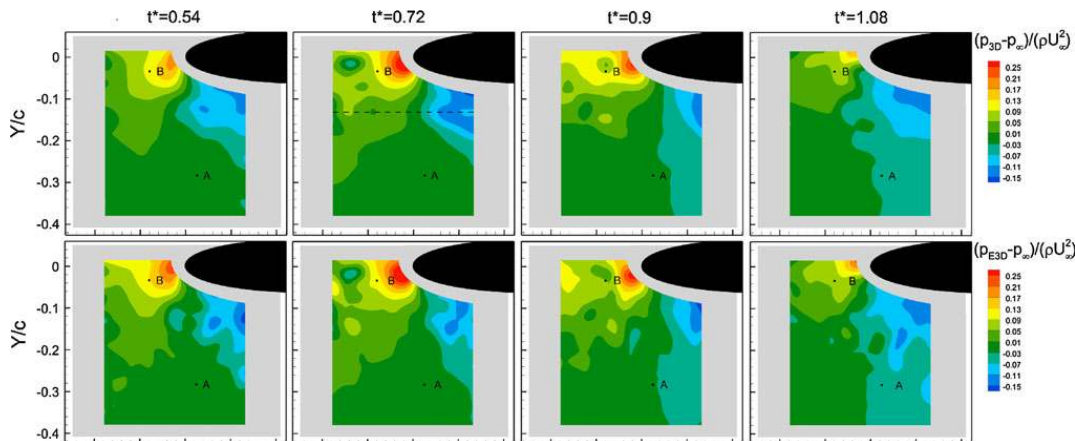

Figure 8. Sequence of pressure fluctuation contours: first row: Lagrangian approach; second row: Eulerian approach (Violato et al. 2011).

In the study of Kat & Oudheusden (2012) a comprehensive investigation was made of the theoretical performance of different pressure-determination procedures, using theoretical considerations as well as synthetic PIV experiments of an advecting Gaussian vortex. In contrast to the study of Charonko et al. (2010), the impact of the pressure-integration method had been found to be minor, only the direct spatial marching being clearly inferior (see also Kat et al. 2010a), but both the Poisson method and the omni-directional approach of Liu an Katz (2006) performed equally well. In view of this, the focus was put on the comparison between the Eulerian and the Lagrangian approach, in relation to the impact of temporal and spatial resolution and the propagation of velocity error in the pressure results.
The accuracy of the pressure determination was expressed in terms of the peak pressure response (i.e. the ratio of the resolved maximum pressure difference in the vortex centre relative to its exact value). As expected, for all methods the results improve with spatial resolution, with a peak response better than 90% when the window size is less than a third of the vortex core radius. Regarding the impact of

the temporal resolution, the analytical analysis suggest that, in view of the different definitions of the Eulerian and Lagrangian time scales, the Eulerian approach will start to degrade for increasing advection velocicty (for a given vortex size), while for the Lagrangian approach the vortex turnover time is the limiting factor. The second trend was indeed observed (see Figure 9-left), and the peak response starts to fall when the time separation becomes larger than 0.1 times the vortex turn-over time. Somewhat surprisingly, the deterioration of the Eulerian approach was not observed in the simulations, as long as the vortex was not placed near the edges of the integration domain. Again the suppression of the error in the time-derivative term of the Euler formulation in the Poisson expression is responsible for this. The time-derivative term only affects the pressure computation through its contribution to the boundary conditions, and indeed the expected dependence of the Euler approach on the advection velocity becomes apparent when the vortex is placed near the edge of the domain. The error propagation was found in good agreement with the theoretical prediction, in that the Eulerian approach has a higher error propagation in the presence of mean flow (effect of advection velocity, see Figure 9-right).

The influence of non-2D flow (out-of-plane motion) was also in this study investigated by inclining the vortex axes with respect to the viewing angle. With proper 3D velocity input (including out-of-plane terms), the pressure is correctly predicted, while with a planar data input the peak pressure falls off as approximately the cosine of the inclination angle, so a 90% peak response at approximately 25 degrees inclination, which agrees well with the outcome of Charonko et al (2010).

Subsequently, the analytical predictions were compared to a real experiment of a square-section cylinder wake, assessing results of Stereo-PIV (planar approach) and thin-volume Tomo-PIV (volumetric approach). The inferred pressures were validated against pressure transducers mounted in the lateral side or at the back of the cylinder. Figure 10 shows an instantaneous flow realisation, as well as comparisons for the pressure time record for the different experiments. It is clear that for the planar approach (Stereo-PIV experiment) the results agree well for the side of the cylinder, where the flow is predominantly 2D, while the agreement is much worse at the back, where the wake has developed strong 3D flow structures with significant out-of-plane motion. The Tomo-PIV experiment shows that substantial improvement is obtained by including the out-of-plane motion influence. This is further substantiated in Figure 11, which shows the effect of the temporal resolution on the correlation between the PIV pressure and the two transducers, which in this configuration are displaced in spanwise direction on either side of the measurement volume. Figure 11-left shows the correlation results for the side pressure obtained in the Stereo-PIV experiment. The grey line at 0.995 represents the correlation between the two pressure transducers themselves, indicating the high level of spanwise coherence of the flow in this region. The PIV pressure results agree well, with a correlation coefficient of 0.98-0.99. Again, the Eulerian approach is not affected by the time resolution, as the flow is predominantly 2D and there are no strong unsteady structures moving over the edge of the domain. The Lagrangian approach, however, is limited by the vortex turnover time, and displays a drop-off at $\Delta t\, U\, /\, D = 0.3$. Figure 11-centre shows the results for the back pressure obtained in the Stereo-PIV experiment. The reduced correlation between the pressure transducers (correlation coefficient of 0.8) is an indication that the flow is much less coherent in spanwise direction, as a result of strong 3D flow structures. The associated out-of-plane motion affects the PIV-pressure determination (the correlation coefficient has dropped to about 0.6), whereas the departure for decreasing temporal resolution is observed for both the Lagrangian and the Eulerian approaches, however for the latter the drop-off occurs at a time separation of $\Delta t\, U\, /\, D = 3$, which is approximately ten times that of the Lagrangian.

Finally, Figure 11-right shows the results for the back pressure in the Tomo-PIV experiment. Excluding the out-of-plane components in the computation gives similar results as for the planar Stereo-PIV experiment, but with the complete 3D flow information the pressure determination is markedly improved for small values of the time separation, because smaller structures can be better resolved. It may be noted further that also the Lagrangian approach shows this improvement, however, meaningful results could only be obtained for the smallest time separation. At larger values the fluid path could not be reconstructed within the measured volume, due to the strong out-of-plane motion. Larger time separation, hence, would require an increase of the volume thickness.
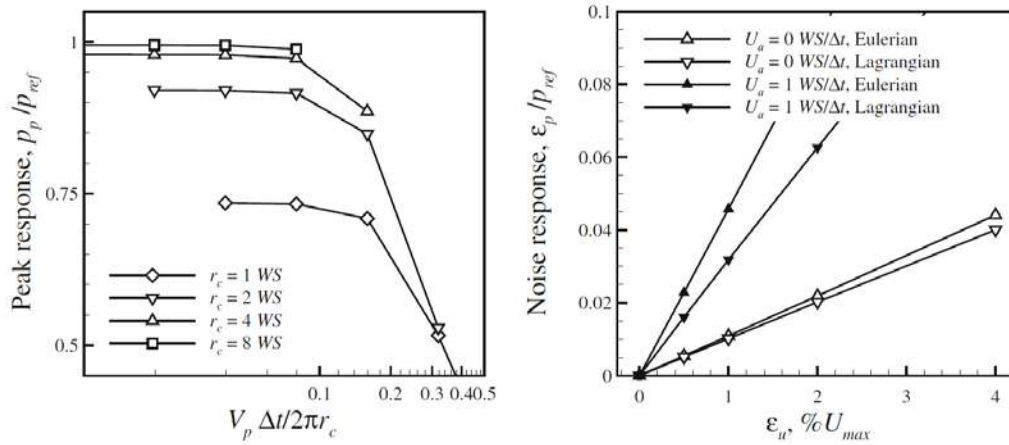
Figure 9. Simulation of pressure determination for a linearly convected Gaussion vortex; left: Peak pressure response with vortex turnover time, Lagrangian approach; Right: Noise response; V_p and r_c are the vortex peak velocity and core radius, respectively (Kat & Oudheusden, 2012).
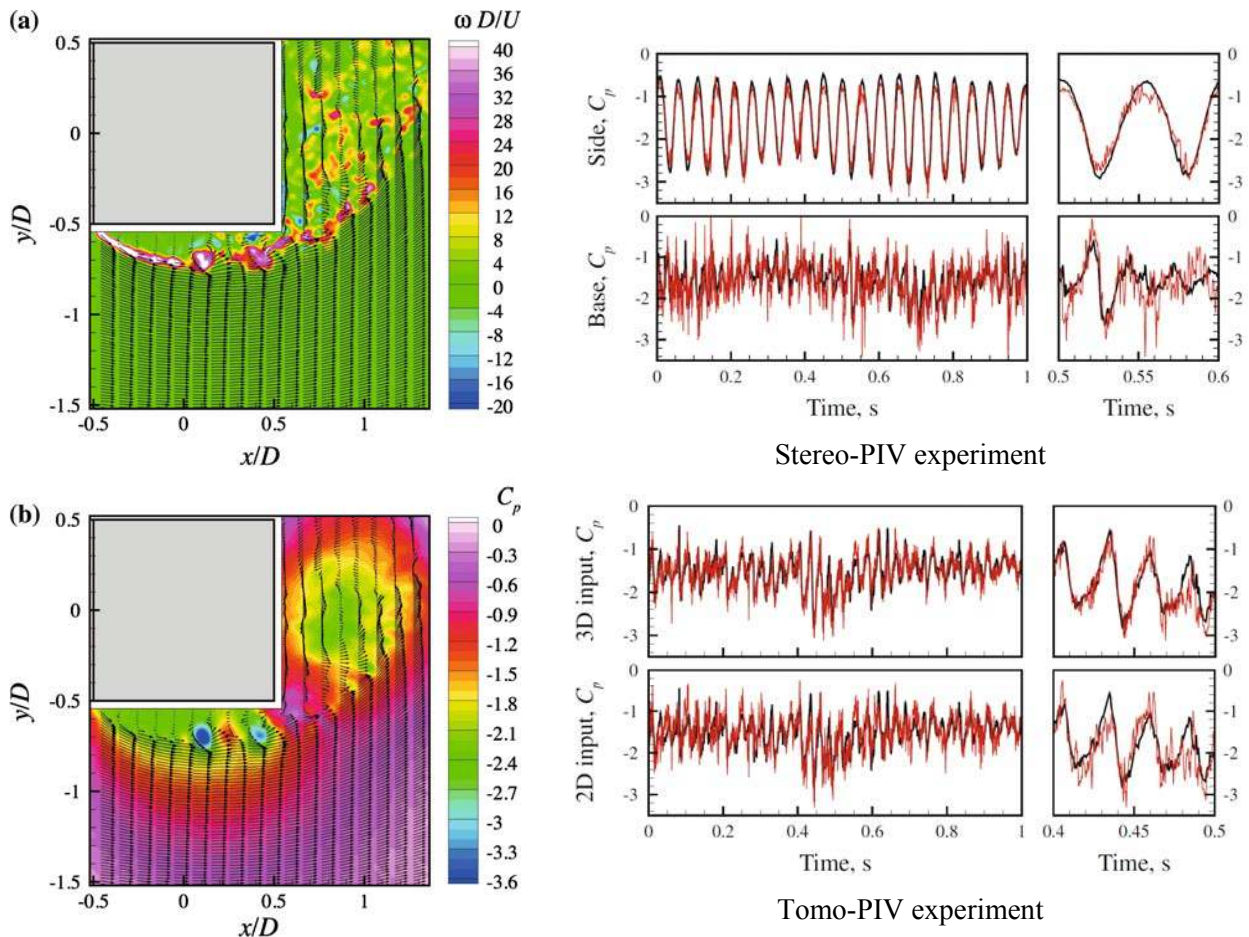

Figure 10. Square-section cylinder experiments (Kat & Oudheusden, 2012): left: sample of Stereo-PIV results (top: vorticity field; bottom: pressure field); right: pressure time records comparison between transducers (black) and PIV-pressure (red).
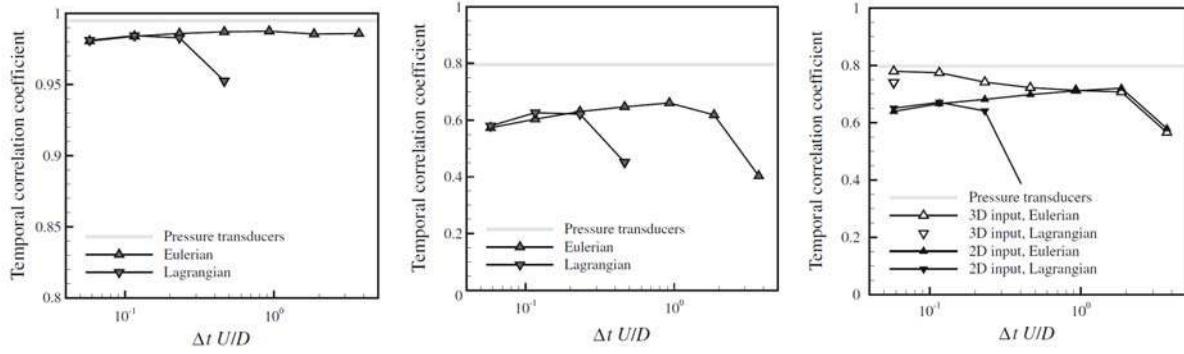
Figure 11. Correspondence between PIV-pressure and transducer reference; left: Stereo-PIV, side pressure; center: Stereo-PIV, back pressure; right: Tomo-PIV, back pressure (Kat & Oudheusden, 2012).

2.8. Phase and Reynolds averaging approaches

The phase-locked measurement approach

When the flow displays a sufficient amount of repeatability over time or when it has a (quasi-) periodic nature, such as in the case of rotary bodies (wind turbine blades, helicopter rotors, aircraft or marine propellers) the direct requirement of temporal resolution may be relieved by deriving "synthetic" time-derivate information from a phase-resolved description of the flow:

$$\frac{\partial <\mathbf{u}>}{\partial t} = \omega \cdot \frac{\partial <\mathbf{u}>}{\partial \varphi} \tag{23}$$

Here <**u**> indicates the phase-averaged velocity and $\omega = d\varphi / dt$ is the phase time-rate-of-change which needs to be known from the experiment parameters. The above procedure has the appealing property that it allows phase-resolved pressure variations to be based on phase-locked measurements that require only a phase synchronisation with the flow phenomenon, but no high framing rate. Hence, the relatively high-performance CCD-based PIV systems can be used even at higher flow speeds, while the phase-locked approach can provide a well-converged data ensemble from which synthetic acceleration data can be obtained with much higher accuracy than when based on individual time-series samples.

Time-mean pressure fields by means of Reynolds-averaging

As reflected by the above discussion a planar pressure field computation under general unsteady flow conditions poses quite a challenge in terms of both the temporal resolution and/or the 3D capability of the PIV measurement. These requirements can be relaxed by treating the flow in a statistical sense and extracting the time-averaged pressure field, which may be a sufficient result for several applications. The mean-pressure gradient is obtained from Reynolds-averaging of the momentum equation, as indicated by the overbar:

$$\nabla \overline{p} = -\rho \, (\overline{\mathbf{u}} \cdot \nabla)\overline{\mathbf{u}} - \rho \nabla \cdot (\overline{\mathbf{u'u'}}) + \mu \nabla^2 \overline{\mathbf{u}} \tag{24}$$

showing that additionally the Reynolds stress terms need to be included, which are obtained from the statistical ensemble of the individual velocity fields. The Poisson approach may be adapted in a similar fashion (see e.g. Gurka et al. 1999), to yield:

$$\nabla^2 \overline{p} = -\rho \nabla \cdot (\overline{\mathbf{u}} \cdot \nabla)\overline{\mathbf{u}} - \rho \nabla \cdot \nabla \cdot (\overline{\mathbf{u'u'}}) \tag{25}$$

Evaluating the in-plane components of the mean-pressure gradient from equation (24) yields:

$$\frac{\partial \overline{p}}{\partial x} = -\rho \left\{ \overline{u}\frac{\partial \overline{u}}{\partial x} + \overline{v}\frac{\partial \overline{u}}{\partial y} + \overline{w}\frac{\partial \overline{u}}{\partial z} + \frac{\partial \overline{u'^2}}{\partial x} + \frac{\partial \overline{u'v'}}{\partial y} + \frac{\partial \overline{u'w'}}{\partial z} \right\} + \mu \left\{ \frac{\partial^2 \overline{u}}{\partial x^2} + \frac{\partial^2 \overline{u}}{\partial y^2} + \frac{\partial^2 \overline{u}}{\partial z^2} \right\}$$

$$\frac{\partial \overline{p}}{\partial y} = -\rho \left\{ \overline{u}\frac{\partial \overline{v}}{\partial x} + \overline{v}\frac{\partial \overline{v}}{\partial y} + \overline{w}\frac{\partial \overline{v}}{\partial z} + \frac{\partial \overline{u'v'}}{\partial x} + \frac{\partial \overline{v'^2}}{\partial y} + \frac{\partial \overline{v'w'}}{\partial z} \right\} + \mu \left\{ \frac{\partial^2 \overline{v}}{\partial x^2} + \frac{\partial^2 \overline{v}}{\partial y^2} + \frac{\partial^2 \overline{v}}{\partial z^2} \right\}$$

(26)

In comparison to equation (9), this shows that a 3D characterization of the mean flow, obtainable for example with multiple-plane 3C-PIV, is a sufficient basis to be able to compute the in-plane mean pressure distribution. Murai et al. (2007) suggest to include a sub-grid model to account for the contribution to the Reynolds stress from turbulent scales that are not resolved by the PIV measurements. They evaluated the impact of this on the measurement of a Savonius rotor and found that the effect on the local pressure coefficient could be up to 12%, whereas the overall contribution to the torque was no more than 3%. They suggest that the effect would increase for larger Reynolds numbers (which was 10^4 in their experiments).

As an example of the use of the Reynolds-averaging concept in a strongly unsteady flow, Figure 12 shows the representation of the mean-pressure gradient from 2C-PIV statistical data for the flow around a square section cylinder, under the assumption of 2D mean flow, as reported in Oudheusden et al (2007). The first diagram depicts the complete pressure-gradient vectors, the others show the contributions of mean momentum ('Euler terms'), Reynolds stresses ('fluctuating terms') and viscous stresses, corresponding to the subsequent terms in equation (24). The viscous terms are seen to be negligible (note strongly magnified scale), whereas the mean flow terms dominate in the flow outside the wake while the turbulent terms are significant in the wake region only. A similar justification for neglecting the viscous term in the momentum equation at sufficiently high Reynolds number was documented by Murai et al. (2007), in their analysis of PTV measurements around a Savonius rotor.
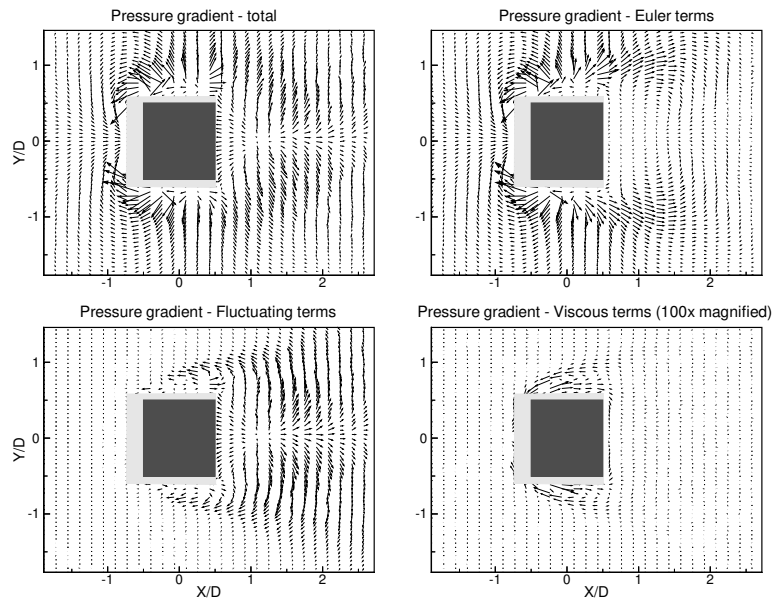

Figure 12. Contribution of different terms to the mean pressure gradient for the flow around a square-section cylinder; $\mathrm{Re}_D = 20,000$, $\alpha = 0°$ (Oudheusden et al. (2007).

3.   More advanced flow-property extraction procedures

The procedures considered in this section have as common denominator that a more elaborate flow model is used in the pressure determination, either to provide extra redundancy for the data processing, or because of the fact that the flow physics is requiring additional aspects to be taken into account (compressibility, body forces).

3.1.   Extension to compressible flows

Also in the case of compressible flow the computation of pressure from the velocity field relies on invoking the flow governing equations, the momentum equation in particular. In many aeronautical applications the assumption of isentropic flow may be valid for a large domain of the flow. Under this assumption, a direct algebraic relation applies between pressure and velocity (similar to Bernoulli's relation for incompressible flow):

$$\frac{p}{p_\infty} = \left(1 + \frac{\gamma - 1}{2} M_\infty^2 \left(1 - \frac{V^2}{V_\infty^2}\right)\right)^{\frac{\gamma}{\gamma - 1}} \tag{27}$$

An example of this approach applies to the transonic airfoil study reported by Ragni et al. (2009). Figure 13 shows the results of the transonic airfoil experiment, on a NACA 0012 airfoil under transonic conditions (M = 0.6). The airfoil chord is 100 mm, further details on the experimental configuration can be found in the original publication. In the present discussion we focus on the extraction of the pressure field around the first part of the airfoil, imaged on a FOV of 50mm×50 mm. In the flow case depicted here the flow remains predominantly steady, permitting ensemble correlation to be applied to increase the spatial resolution. In addition, stream-wise elongated windows were used to further increase the resolution in the wall-normal direction. Final window size was 15×5 pixel at 50% overlap, yielding a vector grid of 0.41mm × 0.14mm.
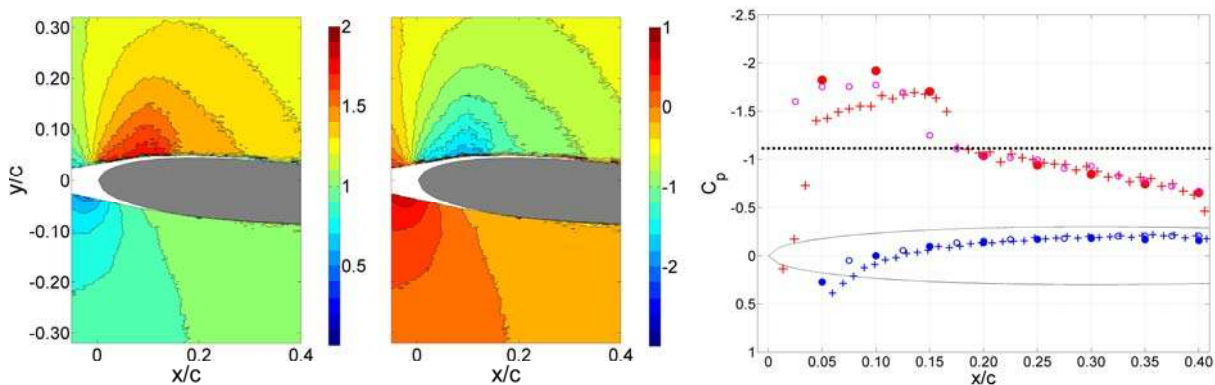

Figure 13. Left: Contours of velocity magnitude and (centre) pressure coefficient obtained from the isentropic relation for α = 4º and Mach = 0.6. Right: Pressure distribution comparison at the airfoil surface (blue: pressure side, red: suction side); +: PIV data extracted at 1 mm (1% chord) from the surface; ○: PIV data extrapolated to the surface; ●: pressure orifices. The dotted black line indicates the critical value of the pressure coefficient (Ragni et al. 2009).

In validation of the PIV-derived pressure data, the right-hand part of the figure presents the pressure distribution over the airfoil, where the dotted black line indicates the critical value of the pressure coefficient. The latter indicates that a supersonic region is present over the front part of the airfoil. Reference surface pressure is provided from pressure orifices. In view of the extremely thin boundary layer the isentropic condition applies up till very near the airfoil surface, however, the PIV measurements close to the surface become unreliable due to reflections and edge effects. Therefore

PIV-based surface pressure distributions are given for data taken at a relatively large distance from the surface (~ 1 mm = 1% chord). This distance introduces a significant deviation from the actual surface pressure when the pressure gradient normal to the surface is prominent, which is especially the case in the leading edge region. When using a linear extrapolation of the PIV data down to the surface, a better match with the measurements from the pressure orifices is obtained. In conclusion, the results show that this extrapolation procedure corrects the PIV based pressure distribution significantly, and brings it to values comparable to the pressure orifices within a few percent.

Clearly the isentropic flow assumption is violated in regions affected by shock waves and in viscous shear layer regions (boundary layers, wakes). An extension of the pressure-integration procedure to compressible flow conditions was described in Oudheusden et al. 2007 and Souverein et al. 2007. They employed again the momentum equation as the fundamental relation for obtaining the pressure gradient, but in the case of compressible flow additional relations must be included to account for the variable density. Secondly, compressible flows display specific flow features, notably shocks but also thin shear layers that pose particular difficulties in the velocity measurement itself, as well as in the subsequent pressure-gradient integration.

In the study of Souverein et al. (2007) a convenient solution approach to account for the density dependence was proposed, by using an adiabatic flow assumption together with the gas law. The first approximation, taking that total enthalpy of the flow is constant, allows a direct relation to be established between temperature and velocity:

$$\frac{T}{T_\infty} = 1 + \frac{\gamma - 1}{2} M_\infty^{\,2} (1 - \frac{V^2}{V_\infty^{\,2}}) \tag{28}$$

This assumption of adiabatic flow is justified, also for viscous regions, in the case of steady flow without significant heat transfer. Secondly, the perfect gas law is invoked to eliminate the density in terms of pressure and temperature, yielding the following relation from which the pressure can be evaluated non-iteratively upon spatial integration (note that the viscous term has been neglected):

$$\frac{\nabla p}{p} = \nabla \ln(p / p_\infty) = -\frac{1}{RT} \cdot \frac{D\mathbf{u}}{Dt} = -\left(\frac{\gamma M_\infty^{\,2}}{V_\infty^{\,2} + \frac{\gamma-1}{2} M_\infty^{\,2} (V_\infty^{\,2} - V^2)} \right) \cdot \frac{D\mathbf{u}}{Dt} \tag{29}$$

The method was subsequently applied in a PIV-based loads determination of an airfoil in supersonic flow, for which purpose the pressure was computed only on a contour surrounding the airfoil. A special shock treatment was applied by first identifying and characterizing the shocks and propagating the pressure information over the shocks using theoretical shock relations. A subsequent study (Oudheusden 2008) showed that straightforward pressure-gradient integration can also be applied to propagate pressure information across shock regions when neglecting the viscous terms, when the momentum equation is used in its conservative formulation. In the case of a turbulent flow the contribution of the turbulent stresses, provided they are properly resolved by the measurement and neglecting the effect of density fluctuations (for moderate Mach numbers), may be included in the pressure-gradient formulation, starting from the Reynolds-averaged form of the momentum equation, similar as in the case for incompressible flow (Oudheusden 2008). The latter publication reports on the determination of the planar pressure field for the supersonic flow around a biconvex airfoil as well as a shock-wave turbulent boundary layer interaction.

3.2.   *PIV-based measurement of body force distribution in plasma actuators*

A related procedure of combining PIV velocity measurements and flow-governing equations in order to extract non-kinematic flow properties, has very recently been addressed, but then with the specific purpose of obtaining information on the body force exerted by a plasma actuator used for flow control. The momentum equation with inclusion of the body force $\mathbf{F}(\mathbf{x},t)$ can be written as:

$$\mathbf{F}(\mathbf{x},t) = \nabla p + \rho \frac{D\mathbf{u}}{Dt} - \mu \nabla^2 \mathbf{u} \qquad\qquad (30)$$

As in this case there are two unknown forces driving the flow material acceleration, the body force and the pressure gradient, which separate effects cannot be distinguished, additional assumptions are needed to extract the body force from the velocity measurements, essentially eliminating the pressure gradient.

The approach reported by Kotsonis et al. (2011) relies on the availability of time-resolved measurements of the temporal development of the velocity field from an initially quiescent situation and the assumption that the body force F remains constant in time. The pressure gradient (taken to be zero at the initial time) can then be evaluated from the integration of the time-derivative of the momentum-equation:

$$\nabla p = -\int_0^t \frac{\partial}{\partial t}\left(\rho \frac{D\mathbf{u}}{Dt} - \mu \nabla^2 \mathbf{u} \right) dt \qquad\qquad (31)$$

Knowing the pressure gradient, the body force can now be computed. The procedure to obtain the body force relies evidently on the correctness of the assumption of constant body force and the availability of a time-resolved PIV data. The results given in Figure 14-a and b illustrate the measured time evolution of the flow field and the estimated body force spatial distribution. Figure 14-c shows the time evolution of the different terms in the NS equation after actuation onset at $t = 0$. It shows how the acceleration term dominates the flow developments in the initial phase, which allows for an approximate estimation of the body force based on this term alone (referred to as the "reduced method"). Convection and pressure gradient eventually become dominant, while viscous effects remain small during the entire actuation period.

(a)

(b)
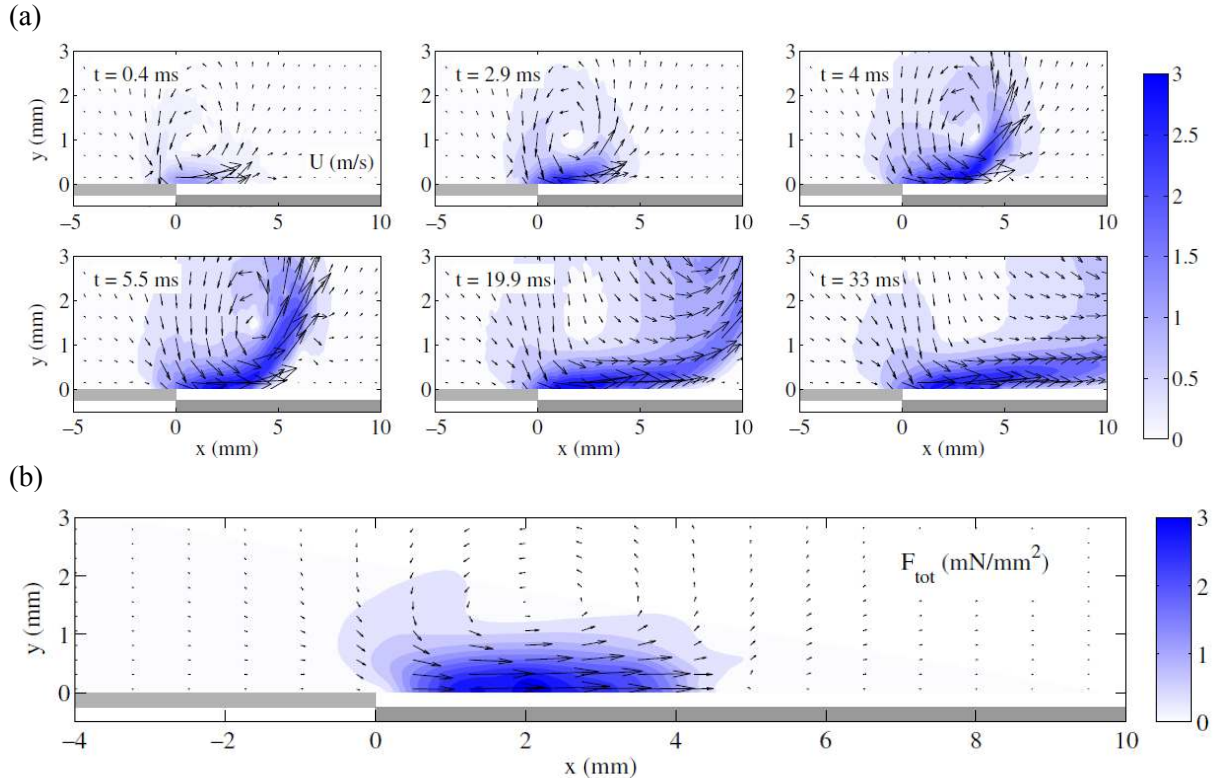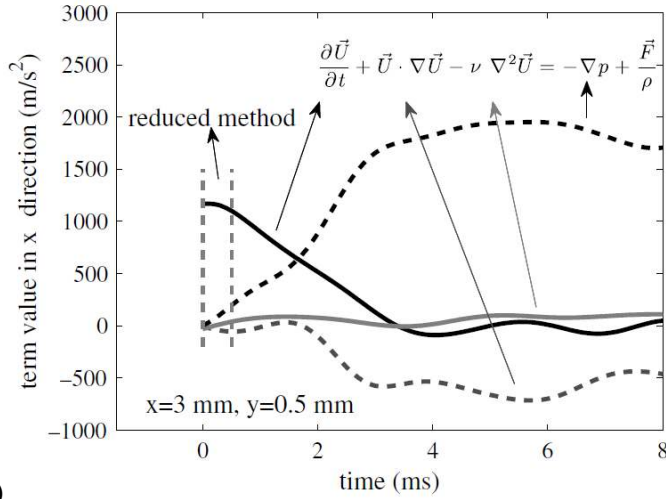
(c)

Figure 14. Analysis of the flow generated by a plasma-induced body force. (a) Temporal evolution of the velocity flow field; (b) computed spatial distribution of the body force, average of results over 20 ms time duration; and (c) the balance between the different terms in the NS equation.(Kotsonis et al. 2011)

As an alternative approach, Albrecht et al. (2011) remove the pressure gradient by taking the curl of the momentum equation, which allows the curl of the body force to be expressed in terms of the transport of vorticity, $\omega = \partial v / \partial x - \partial u / \partial y$, yielding:

$$\frac{\partial F_x}{\partial y} - \frac{\partial F_y}{\partial x} = \rho \frac{D\omega}{Dt} - \mu \nabla^2 \omega \qquad (32)$$

Additionally, in view of the elongated configuration of the plasma actuator, the forcing is assumed to be mainly in the streamwise (x) direction, which leads to the approximation that $\partial F_x / \partial y \gg \partial F_y / \partial x$.

This allows the streamwise component F_x of the body force to be obtained from integration in the wall-normal direction y, taking as boundary condition that the body force is zero far from the wall. Although attractive as the method does not require time-resolved data, significant errors are introduced in the areas where $\partial F_y / \partial x$ is important, such as near the edges of the actuator.

3.3.   Data assimilation and pressure determination through PIV-CFD synergy

All previous approaches to determine the pressure (or other flow parameters) from PIV can essentially be viewed as post-processing procedures, in which the PIV velocity data, obtained from the correlation of particle images, is taken as input for the computation of the pressure by application of the momentum equation. A number of studies, however, have proposed a more intimate connection between image-processing and pressure determination or between PIV measurement and CFD flow simulation.

As recognized by several investigators, the derivation of the pressure from a velocity solution through use of the Poisson equation is a common element in many iterative CFD solution methods. Standard CFD-like approaches for solving the Pressure-Poisson problem were, hence, applied by Hosokawa et al. (2003) and Jaw et al. (2009), on the basis of the SOLA and SIMPLER solution schemes, respectively. Apart from providing the pressure field, these methods also provide the possibility for a velocity data regularization, i.e. to "correct" the measured velocity accordingly and to remove unphysical vector outliers.

25

In recent years the concept of data assimilation has been explored as a means to derive additional flow properties in connection to PIV measurement data. Essentially, this coupling of CFD and PIV implies that, given a measured velocity field in space, the CFD provides the most likely solution of the entire flow field, including the non-measured properties. Although the major principle problems of combining CFD and PIV appear to be the validity (or appropriateness) of the theoretical model and the boundary conditions (Regert et al. 2011), specific activities have been undertaken in this field recently (Lemke and Sesterhenn 2012).

Whereas these methods still rely on PIV velocity data obtained from the local cross-correlation of sub-elements of the particle images (interrogation windows), a different class of procedures have been considered, where also the image interrogation itself is included in the synthesis with CFD. Okuno et al. (2000) describe a so-called physics-constrained image interrogation procedure. Rather than separately computing the velocity field from correlation of the particle images, after which the pressure is obtained in a second step using the flow governing equations, the image interrogation is treated as a multiobjective optimization problem, where the velocity field is constrained to obey the flow-governing equations of continuity and momentum, where in the latter case the pressure is obtained as a direct result of the image analysis. The velocity is, hence, obtained by minimizing a measure which consists of the residues of the momentum and the continuity equation, and the difference between estimated and observed image data. The resulting non-linear optimization system was solved iteratively, using methods from evolutionary programming, until the difference between the observed and the estimated image is considered sufficiently small. The method was demonstrated on an impinging jet flow, a cavity flow (see Figure 15) and the flow around a waving airfoil. Ruhnau and Schnorr (2007) present a somewhat similar physics-restrained analysis of the particle images, but then in the context of the optical flow principle. In their particular study, the flow physics model was that of a Stokes flow. Also Regert et al. (2011) discuss the possibilities of integrating the pressure determination at the level of the image analysis.
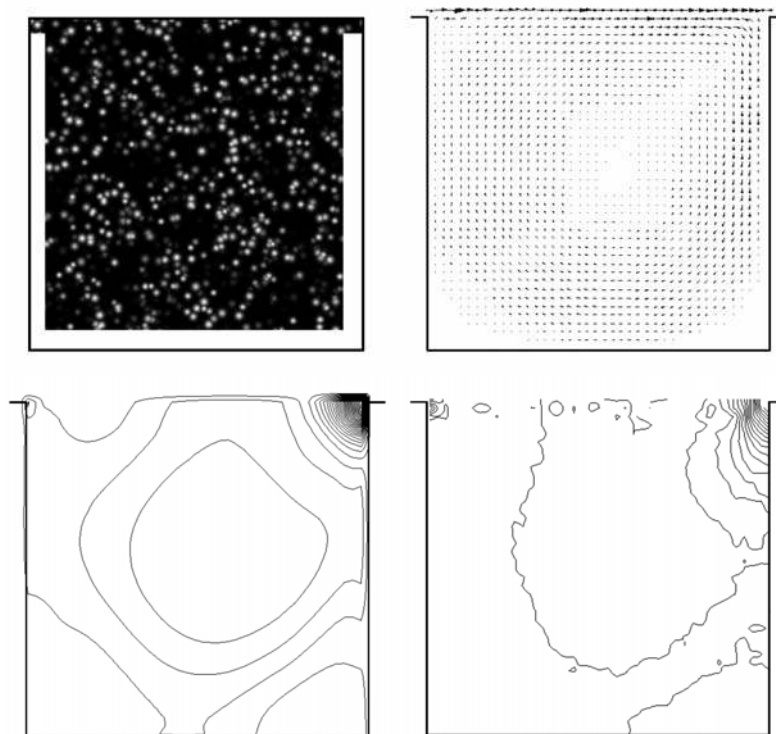

Figure 15. The physics-constrained image interrogation procedure of Okuno et al. (2000) applied to a cavity flow. Top: example of particle image and extracted velocity field; bottom: exact and extracted pressure field.

4.   Application areas

The predominant interest for pressure fields usually lies either in the domain of unsteady fluid-dynamic phenomena or in the relevance to the aerodynamic or hydrodynamic loads that act on immersed objects or on the walls of a flow channel. As stated, the specific focus of this review is associated to the particular capabilities of PIV-based pressure determination in unsteady flows. Steady (or time-averaged) pressure field determination has been applied e.g. by Gurka et al. (1999) to a nozzle flow and an air jet and by Hosokawa et al. (2003) for determining the pressure around a single particle suspended in the laminar pipe flow of a water-glycerine solution and for a single bubble rising in silicon oil. Both studies used the Poisson approach for computing the pressure. In relation to jet flow applications, Fujisawa et al. (2004) used a Reynolds-averaged Poisson equation, following Gurka et al. (1999), in order to determine pressure in the interaction of two parallel jets at different velocities. Vanierschot and Bulck (2008) extracted the planar pressure field in the initial merging zone of an annular swirling jet based on stereo-PIV measurements. The pressure field is obtained numerically from solving the Poisson equation, assuming axisymmetry of the flow. Further internal flow applications include the study of Fujisawa et al. (2006) in relation to the use of micro-PIV in a microchannel junction flow and the use of PIV to determine relative pressures in a stenotic phantom study by Khodarahmi et al. (2010), where PIV was used in a contraction model simulating a stenosis in a human artery.

4.1.   Turbulent flows

The application of pressure determination in unsteady turbulent flows, for which there is often no experimental alternative to obtain instantaneous pressure information, poses particular challenges in view of the relatively small magnitude of the pressure fluctuations and their broad frequency range. The unsteady pressure plays an important role in several fluid-dynamic phenomena, such as cavitation and turbulence, where pressure fluctuations are involved in the transfer of energy between different components of the velocity fluctuations (pressure-velocity correlations) and noise generation (aeroacoustics). Several studies have, hence, explored the potential of using PIV to non-intrusively obtain pressure in synchrony with the flow velocity.

Baur and Köngeter (1999) investigated the pressure in instantaneous vortical structures that are shed in the shear layer behind a surface mounted obstacle. The specific interest of the study was motivated by vortex cavitation inception in separated flow. The investigation was carried out in a 4 cm water tunnel, at a reference inflow velocity of 6 m/s. A high repetition rate PIV system was employed, consisting of a high-speed video camera at a recording rate of 9000 fps and a laser system delivering pulses of 50 μs duration, providing high time resolution of the flow under investigation. Temporal smoothing was applied over 3 consecutive frames, corresponding to a time averaging interval of $\Delta t = 0.33$ ms. Time-series samples are given in Figure 16 (top row), showing velocity vectors superimposed with vorticity field contours. The two circles indicate identified regions of clockwise-rotating vertical motion, that were suggested to be related to horseshoe vortices. Using the integration scheme described previously, instantaneous pressure fields were obtained by spatial marching, averaging results from downward and upward marching with time-mean pressure values as initial input, see the original publication for details. The authors state that "The chosen approach yields a combination of unsteady pressure calculation with steady boundary conditions. This shortcoming has to be accepted because no other method seems to be practical."
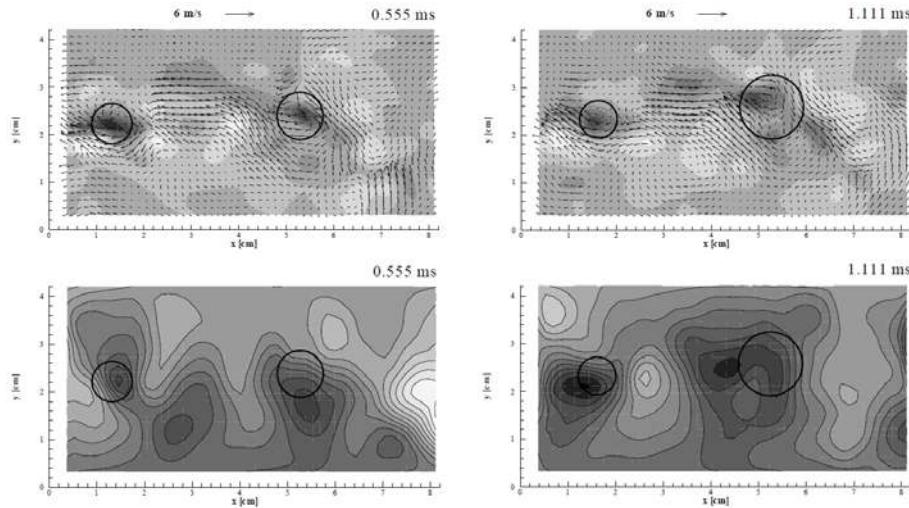
Figure 16. PIV measurements of a shear layer behind a surface mounted obstacle; top: velocity fields with vorticity contours; bottom: pressure contours; the circles indicate identified vortical structures (Baur and Köngeter 1999).

In a series of studies Liu and Katz (2006, 2007, 2008) have reported extensively on the investigation of cavitation in a cavity flow by means of a dual-PIV system, consisting of 2 lasers and 2 cameras, with each system separated by orthogonal polarization. The PIV system is operated such that 4 pulses at 25 μs separation are delivered, which are subsequently used to derive the material acceleration. Integration is performed by the omni-directional approach outlined in detail in Liu and Katz (2006). In a subsequent study (Liu and Katz 2007), they applied the method to obtain statistics on pressure fluctuations and pressure-velocity correlations, allowing to draw conclusions on the cavitation phenomena that occur as a result of the interaction of the shear layer vortices with the trailing corner of the cavity, see Figure 17 (Liu and Katz 2007, 2008).
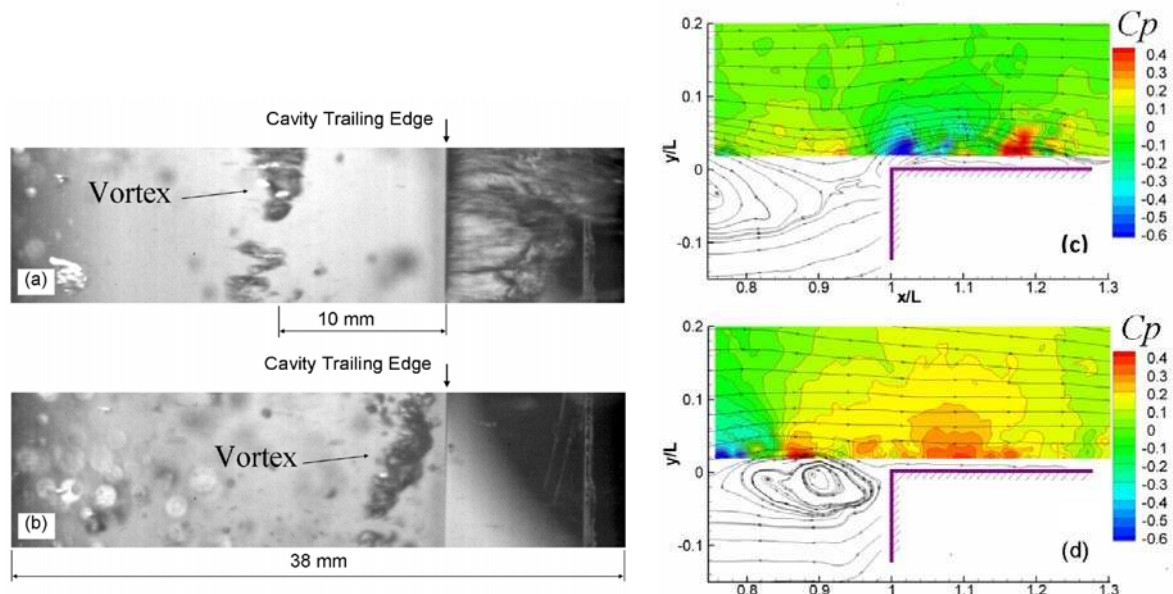

Figure 17. Cavitation in a water flow (Liu and Katz 2008). The top view visualizations in (a) and (b) give evidence of extensive cavitation above the corner when the vortex is located 10 mm upstream of the corner and its disappearance near when the vortex approaches the corner; (c) and (d) show sample instantaneous flow patterns and corresponding pressure distributions for moments with either high or low pressure above the corner.

A further study of cavitation was reported by Chang et al. (2011), to investigate the possible suppression of tip vortex cavitation by active mass injection, while other researchers have addressed cavity flows in particular relation to cavity acoustics (see next section).

Some recent studies have employed high-speed PIV for a time-resolved characterization of the instantaneous pressure in turbulent boundary layers. Joshi et al (2012) investigated the effect of boundary-layer-scale fluctuating pressure gradients on the turbulence structure of ZPG and FPG boundary layers. The investigation was carried out in an optically-index matched water facility (flow speed 1-2 m/s) and a high-speed 2C PIV system is used to acquire planar image data at 5000 fps. The pressure data obtained are filtered in time and space to provide boundary-layer-scale data, which justifies using a two-dimensional pressure approach. The flow is conditionally averaged, in relation to the instantaneous streamwise pressure gradient and the impact of pressure gradients on vorticity production and transport is addressed. Ghaemi et al. (2012) applied a time-resolved PIV system to investigate pressure fluctuations in a turbulent boundary layer at a free stream velocity of 9.3 m/s and a momentum-based Reynolds number of 2,400 (the boundary layer thickness is 31 mm). A 2C-PIV system was applied to characterize the turbulent boundary layer, as well as for the evaluation of the pressure field from time-resolved planar measurements. Additionally, a tomographic PIV experiment was carried out, for which the laser sheet thickness was expanded from 1 mm (as used for the 2C-PIV) to 3.5 mm in the spanwise direction. The pressure is evaluated from the time-resolved (planar or tomographic) PIV data fields acquired at 10 kHz in continuous mode and validated against surface-installed microphones mounted behind a pinhole orifice. The comparison shows agreement between the two signals with a cross-correlation coefficient of 0.6, while the power spectral densities overlap up to 3 kHz for the tomographic data, and up to 1 kHz for the planar method, see Figure 18. The visualization shows a snapshot of pressure fluctuations above the wall, identifying three vortex heads labelled A to C, as supported by the Q-level contours and relative flow motion in the convective reference frame.
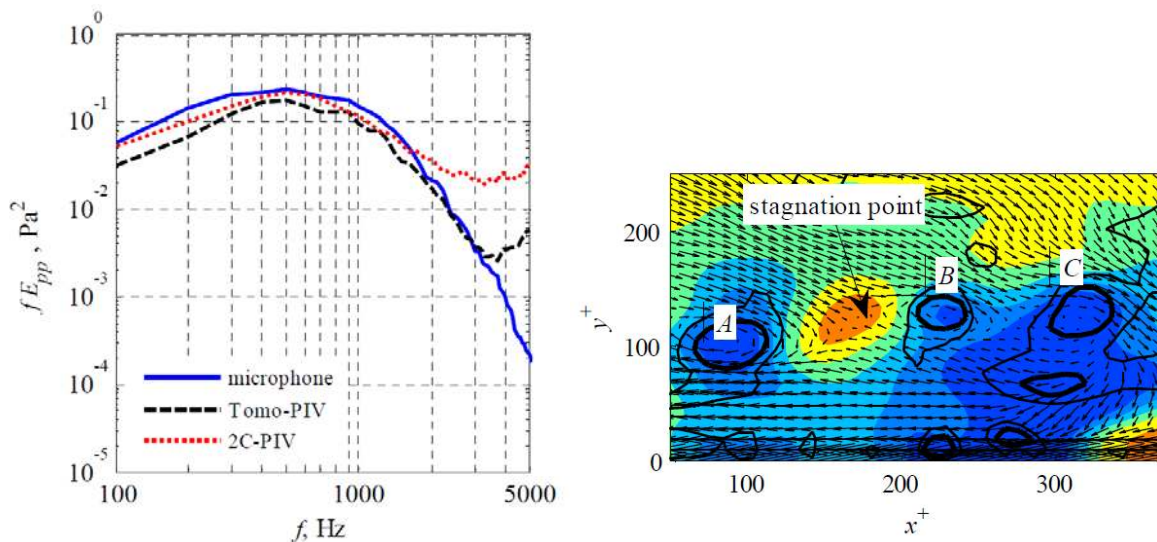

Figure 18. Pressure determination in a turbulent boundary layer (Ghaemi et al. 2012). Left: the pre-multiplied PSD of the wall-pressure, with comparison between planar and volumetric PIV and reference microphone data. Right: snapshot of pressure fluctuations (colour contours) together with vortex visualization based on contours of Q-criterion and velocity vectors in relative convective frame.

Further application of PIV-based pressure determination in a turbulent boundary layer was reported by Proebstein et al. (2012), with a validation against both a surface microphone and DNS simulation data. Also in this case a flat-plate boundary layer was considered, however at a reduced thickness of 10 mm (corresponding momentum-based thickness is 720). Planar PIV was used to characterize the boundary layer, while the tomographic configuration was now aligned with the wall, with dimensions of the measurement volume being $2.2\delta \times 4.5\delta \times 0.5\delta$ in the streamwise, spanwise and wall-normal direction, respectively. The enhanced spanwise extent was motivated by the specific objective of the study, which was to obtain information on the spanwise coherence length of the pressure fluctuations, as required for the acoustic prediction of trailing edge noise.

4.2. *Aeroacoustics*

A further application of time-resolved PIV data for unsteady pressure determination lies in the field of aeroacoustics. According to the theory developed by Lighthill, the acoustic emission is governed by a wave equation with acoustic sources and the time-resolved, three-dimensional capabilities of PIV offer new opportunities to quantify aeroacoustic problems by providing the input for sound prediction based on acoustic analogies. PIV was used by Schröder et al (2006) for the investigation of trailing edge noise sources, while jet-noise produced by vortex pairing was investigated by Schramm et al. (2004) and Violato et al (2010). Henning et al. (2008) and Uda et al. (2011) investigated the aeroacoustic noise generation of cylinder wakes by a combination of PIV flow field measurement and microphone recording of the radiated sound. Also Kastner et al. (2009) report on the combined use of PIV and a microphone array, to investigate the relation between flow fluctuations and sound generation in a subsonic jet.

In the case when the noise production is dominated by the presence of scattering surfaces, such as in the case of cavity noise, pressure surface fluctuations are required for the acoustic prediction input (Curle's analogy). Murray et al (2007) studied cavity flows in which they used PIV fields acquired in synchrony with high-speed surface pressure transducer data, from which high-speed PIV fields were reconstructed using an Linear Stochastic Estimation (LSE) procedure. The Poisson approach was subsequently used to determine the unsteady pressure fields in relation to the cavity acoustics behaviour.

A cavity flow investigation using high-speed PIV was reported by Haigermoser (2009). The experiments were carried out in a water tunnel with 2D cavities of aspect ratio L/H of 3 and 4. A planar PIV configuration was used, employing a continuous illumination with a 6 W Argon-Ion laser while images were captured with a 1 Megapixel CMOS camera at a recording rate of 1000 fps. From the PIV data, pressure fields were obtained by the integration of the material acceleration, following the procedure of Liu and Katz (2006). The time separation for computing the acceleration was taken as 0.004 s, corresponding to a separation of four frames in the velocity field sequence, in order to reduce the noise on the acceleration computation. The pressure data (typical results shown in Figure 19) are subsequently used for the prediction of the sound emission from the flow. The main source sound was found to be located at the cavity trailing edge and is due to the impingement of vortices shed in the shear layer. Also, it is shown that the flow emits sound with a main directivity in the upstream direction for the smaller aspect ratio, while the directivity is more uniform for the larger aspect ratio. For the larger aspect ratio the acoustic pressure spectrum is also broader, which is attributed to the effect of the downstream circulation zone on the shear-layer instabilities, by destroying their regular pattern.
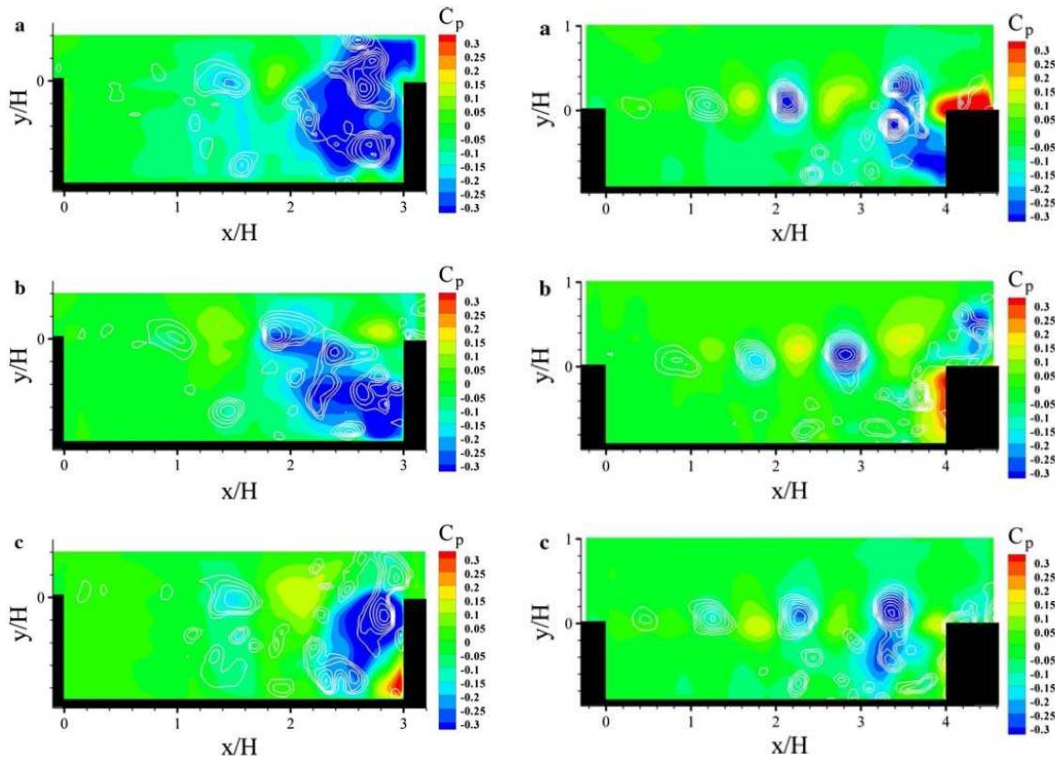
Figure 19. Instantaneous pressure fields in a cavity flow (Haigermoser 2009); pressure coefficient levels (colour contours) and swirling strength (isolines); left L/H=3, right L/H=4.

Also the study reported by Liu and Katz (2011) considers the analysis of the acoustic behaviour of a 2D cavity flow in a water channel, with interest in the pressure field generated by vortex-corner interactions of the shear layer. Time-resolved PIV at an image sampling rate of 4500 fps provided the basis of instantaneous pressure determination, allowing to elucidate the relation between flow phenomena and noise production. Two mechanisms with distinct characteristic frequencies were observed. One is associated with the streamwise transport of the large shear layer vortices, the other with low frequency undulations of the entire shear layer.

Koschatzky et al. (2011ab) describe an investigation of the acoustic emission over an open rectangular cavity in air (aspect ratio L/H = 2, free stream speed 12 and 15 m/s), in which high-speed 2C PIV is employed in combination with wall pressure and direct sound measurements. The PIV image pairs were acquired at a frequency of 3 kHz. The fluctuating pressure fields computed from the time-resolved PIV measurements subsequently serve as input for sound emission prediction. The pressure on the cavity wall and the measured sound are used in assessing the validity of this approach. The study demonstrated the feasibility of this method to quantify the acoustic emission from the cavity, especially for capturing the tonal components. The highest fluctuations in wall pressure occur near the stagnation region on the rear wall of the cavity, where the shear layer impinges. In this region there is a very good match between PIV-based pressure and surface microphone data (see Figure 20-a), whereas away from this region the broadband signal from PIV is too high, which is attributed to represent the accuracy level of the PIV velocity measurement. Figure 20-b displays the acoustic pressure field and sound pressure level above the cavity, as predicted from the acoustic analogy. The points labelled A and B represent locations where microphone measurements were carried out to validate the PIV results (see the original publication for details). In a later experiment (Koschatzky et al. 2012) a comparison was made between 2D and 3D approaches for the sound emission prediction, using a thin-volume tomographic PIV approach. The conclusion was that for this specific flow configuration, where the main source of sound is determined by large span-wise coherent flow

structures, the thin-volume tomographic PIV measurements do not seem to add relevant information to the computation of the sound emission with respect to a planar representation.
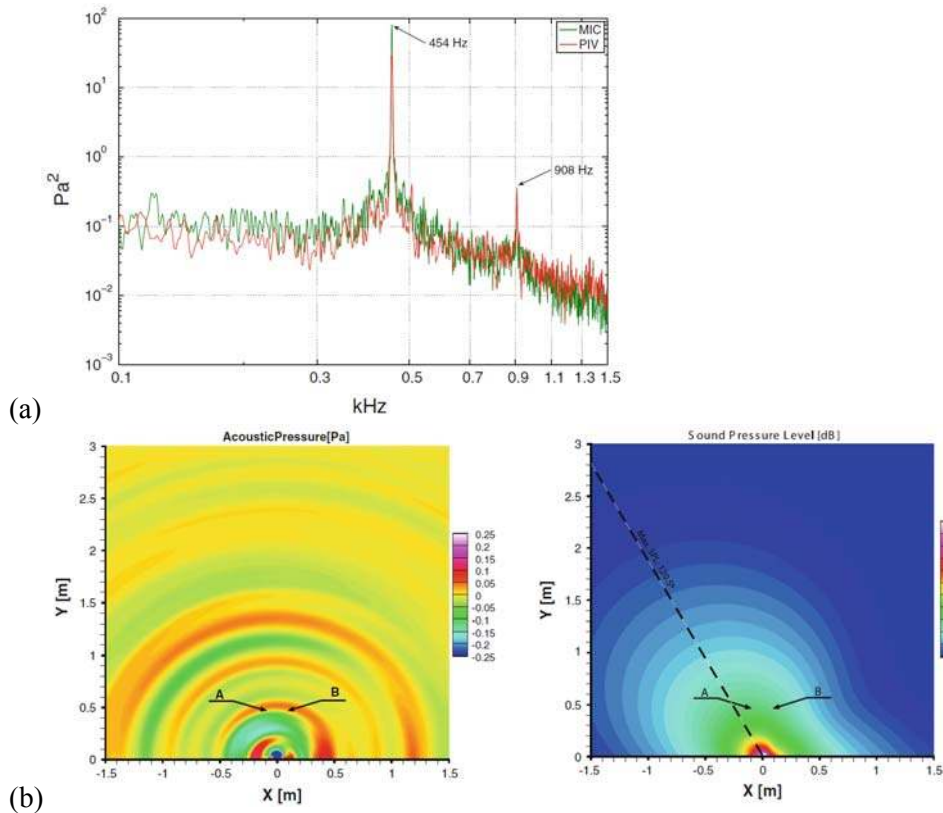

(a)

(b)

Figure 20. Cavity acoustics; (a): pressure power spectra comparison at the location of shear layer impingement; (b) predicted acoustic emission: acoustic pressure field (left) and sound pressure level (right); flow velocity is 12 m/s (Koschatzky et al. 2011a).

The acoustic sound generation by an airfoil placed in the vortex wake of a cylindrical rod (rod-airfoil configuration) was studied with planar PIV by Lorenzoni et al. (2009). Combined PIV and acoustic measurements were carried out in an anechoic wind tunnel at a flow speed of 15 m/s. The use of time-resolved 2C-PIV was motivated by the nominally two-dimensionally geometry of the problem. The pressure was evaluated from the time-resolved PIV data. The pressure at the surface, which constitutes the dipole term in the acoustic analogy, was shown to be responsible for most of the noise emission. The comparison with simultaneous microphone measurements confirmed the ability of the method to resolve the tonal peak and the narrow band spectrum around it (see Figure 21). The high-frequency component of the spectrum, however, was largely overestimated when full spanwise coherency was assumed. Agreement was much improved when the measured coherence length was incorporated in the sound prediction (Lorenzoni et al. 2012). Further elaboration of the acoustic prediction procedures was considered in Moore et al. (2011).

The experimental uncertainties associated to the lack of 3D flow information in the pressure reconstruction and the limited time resolution of the velocity data acquisition were addressed in an improved experiment, described by Violato et al. (2011), using a thin-volume tomographic PIV operating at increased acquisition frequency, see also section 2.7. The effect on the noise prediction of these improved experimental conditions were reported in Lorenzoni et al. (2010). Although the shed vortices shows non-negligible 3D components, which intensify at the interaction with the airfoil, a comparison of the power spectra at the surface revealed only minor 3D motion effects over the entire bandwidth.
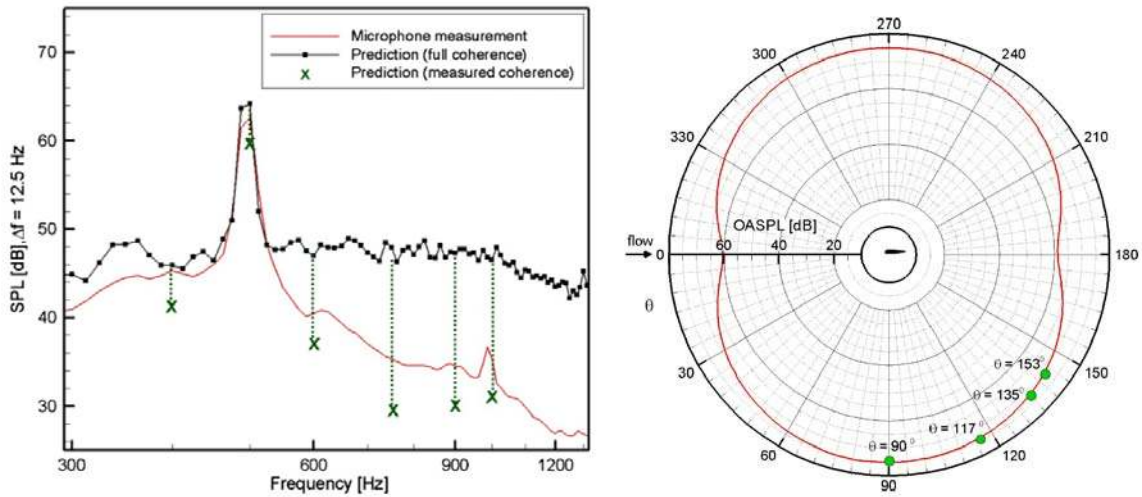
Figure 21. Lorenzoni et al. (2009 and 2012): rod-airfoil acoustics; comparison of measured and predicted sound spectra at one of the microphone positions (left) and polar plot of the overall sound pressure level, the circles indicating microphone data (right).

4.3.   Unsteady separated flows

4.3.1. Oscillating circular cylinder

Fujisawa et al. (2005) report an experimental study of the flow around a circular cylinder, with the specific interest for the effect of a rotational oscillation of the cylinder on the unsteady flow behaviour (vortex shedding) and the forces on the cylinder. The experiment was carried out in a closed-circuit water tunnel, with a Reynolds number of 2000 based on the cylinder diameter of 15 mm. The instantaneous pressure field and fluid forces on the cylinder were derived from the instantaneous PIV velocity data, through solving the pressure Poisson equation with an SOR scheme. The specific approach taken was to combine the Neumann condition on the cylinder surface with uniform pressure at a far field boundary:

$$r = r_1 = R: \quad \nabla p = -\rho\,(\mathbf{u}\cdot\nabla)\mathbf{u} + \mu\nabla^2\mathbf{u}$$

$$r = r_2 \qquad p = p_\infty$$

(33)

It may be observed that through this specific approach, no acceleration information is required. A computational verification showed that a correct prediction of the drag would require the outer boundary r_2 to be placed at a distance of at least 5 diameters from the cylinder. To reconcile this large field of view requirement with that of having sufficient resolution in the flow near the cylinder, a two-camera system approach was adopted. This was implemented by using two CCD cameras (each of 8 bits, 1008×1018 pixels) placed side-by-side with a small off-axis angle (less than 5 degrees), performing simultaneous measurement of the velocity near and far field. One camera is used for the flow observation near the cylinder surface covering an area 35 mm×35 mm and the other is for the far field covering an area 115 mm×115 mm, which is made possible by using a different focal length lens for each camera. The diagrams in Figure 22 show a typical example of instantaneous velocity vectors of the near and far field of the circular cylinder and those of the whole flow field, respectively. The latter is obtained by combining the velocities of near and far fields together, which are processed by interpolation to fit the computational circular grid used for the pressure Poisson equation. Velocities outside the area of measurement are prescribed equal to the free stream velocity.

Some of the findings of the study (see also Figure 23) were that the drag force on the circular cylinder is magnified at low-frequency oscillation and reduced at high-frequency oscillation. The drag coefficient at high-frequency oscillation is reduced by 30% with respect to the stationary cylinder,

while the fluctuating lift is slightly increased due to the generation of synchronized vortex shedding at high-frequency oscillation.
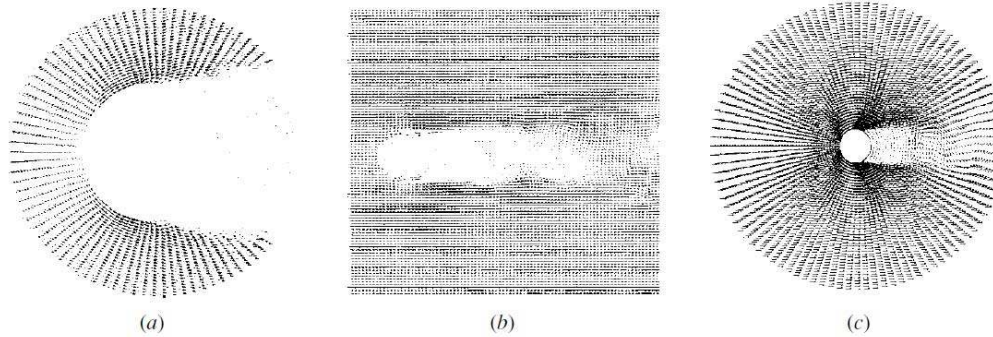

Figure 22. Construction of velocity field for pressure evaluation. (a) Near field, (b) far field and (c) combined velocity field (Fujisawa et al., 2005).
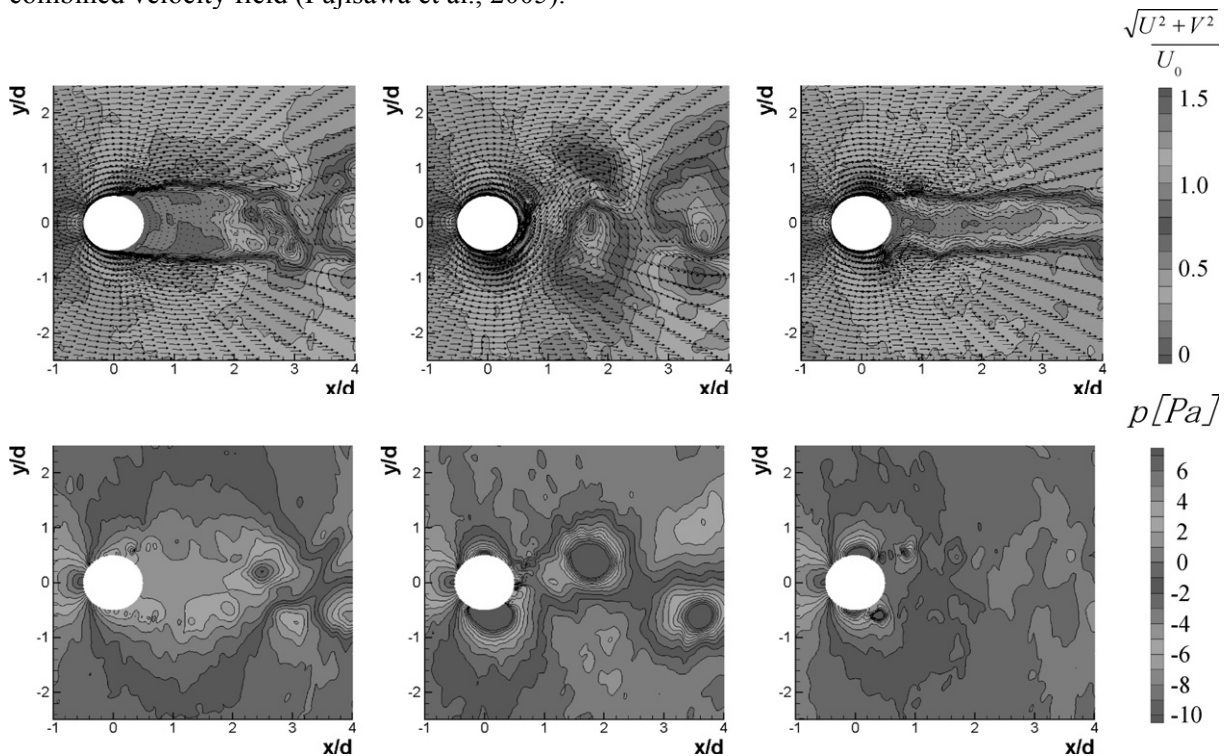

Figure 23. Instantaneous velocity fields (top) and pressure fields (bottom) around a circular cylinder; (*left*) Stationary cylinder, (*center*) low-frequency oscillation (*St* = 0.2) and (*right*) high-frequency oscillation (*St* = 1) (Fujisawa et al., 2005).

4.3.2. Unsteady pressure field around a square section prism

In Kurtulus et al. (2006) the flow around a square-section prism was investigated by means of time-resolved PIV, using a high-repetition rate laser operated at 1 kHz. The particular interest was in obtaining time-varying loads by means of a control-volume approach, for which the instantaneous pressure on the control volume contour was computed from the velocity information. For the pressure determination, a spatial integration of the pressure gradient was applied. As the process of spatial integration is likely to suffer from error propagation, a procedure was proposed that limits the latter

effect by applying the integration only in the wake area, and using the Bernoulli equation outside the wake. The wake is identified based on a threshold on acceleration and vorticity.

A similar experimental configuration was considered by Kat et al. (2008), to determine instantaneous planar pressure fields from time-resolved stereo-PIV with the specific aim of comparing the spatial integration and Poisson approaches, as well as validating these results against reference surface pressure data. For the latter purpose the model was equipped with a pressure orifice and a microphone in close proximity along the centreline of the model, providing reference values for the mean and the fluctuating surface pressure, respectively. In a later study (Kat and Oudheusden 2012), the microphones were replaced with pressure transducers for absolute pressure reference, while also a thin-volume tomographic-PIV configuration was used to allow for the inclusion of the 3D terms in the pressure determination. An example of an instantaneous pressure field has been shown already in Figure 9, while more extensive comparisons between instantaneous and phase-averaged result can be found in Kat et al. (2010b) and Kat (2012). A volumetric visualization of the phase-averaged pressure is depicted in Figure 24, showing the alternating regions of high and low pressure associated to the large-scale vortex shedding.
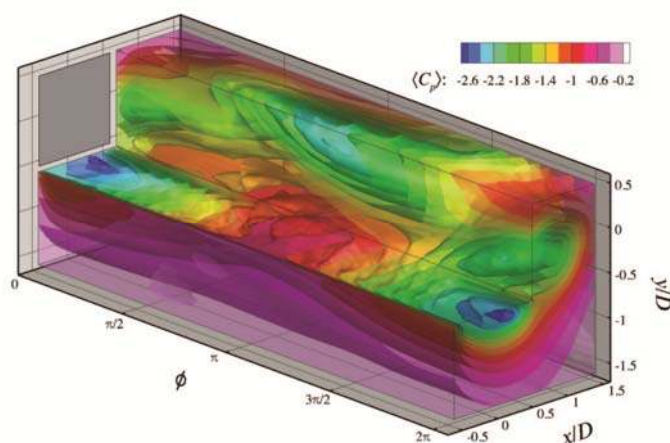

Figure 24. Volumetric visualization of the phase-averaged planar pressure field around a square-section cylinder at Re = 9,500; ϕ indicates the vortex-shedding phase (Kat 2012).

4.4. *Wings and rotors*

Quite a number of studies have explored the potential of using velocimetry data as non-intrusive means for determining pressure fields around wings and other aeronautical or marine application, often with a primary interest in obtaining the fluid-dynamic loads. Oudheusden et al. (2006) have reported the load characterization (both lift and drag) of a NACA642A015 under incompressible flow conditions using planar PIV and a contour-volume approach for computing the aerodynamic loads from the PIV data. The results were validated against standard methods using pressure information obtained from surface pressure orifices and wake-rake data. Very good correspondence was found especially for the pre-stall regime. Fujisawa and Oguma (2008) have reported the time-mean pressure field around a NACA0018 airfoil at 6 degrees incidence, as obtained from PIV data with a comparison to surface pressure data. They employed a Reynolds-averaged form of the Poisson equation, compare section 2.8. Interestingly, they found that inclusion of the turbulent terms, i.e. the contribution of the Reynolds stresses in equation (25), provided a marked improvement in the surface pressure distribution, whereas in the study of Oudheusden et al. (2006) no substantial contribution of the turbulence terms had been detected.

A similar airfoil investigation under transonic conditions was carried out by Ragni et al. (2009) on a NACA 0012-30 at M = 0.60 and Reynolds chord number 2.2×10^6. Again, surface pressure data and wake rake pressures were obtained to allow for a validation of the PIV based pressure and loads results. Results with a reduced size FOV to investigate the LE region in particular have been shown in Figure 13. For the evaluation of the entire flow field a larger FOV was applied of about 1.5 times the chord length. For the results the reader is referred to the original publication. As another application in the transonic regime, Sjörs and Samuellson (2005) present a procedure to obtain the total-pressure variation in the wake of a transonic airfoil from PIV measurements, by integration of the out-of-plane component of the vorticity. The method was tested on a Saab 7301 airfoil at 4 degrees of incidence, with a Mach number of 0.5 or 0.6. The PIV measurements were performed in the wake of the airfoil at a distance of about 0.65 chord lengths downstream of the trailing edge.

Analysis of the unsteady flow fields around moving wings, with particular emphasis on the contribution of pressure to the determination of the aerodynamic loads, have been considered by Hong and Altman (2008), Jardin et al. (2009ab), David et al. (2009) and Rival et al (2010ab), all based on the assumption of (quasi-)2D flow. Pressure fields for the flow along a flexible membrane were reported by Kunze and Brücker (2011). Suryadi and Obi (2011) applied phase-locked stereo-PIV measurement of multiple planes to determine the pressure field and dynamic loads on a rigid plate in a rotational flapping motion. Three-dimensional flow field visualization of velocity and, subsequently, pressure around a 3D flapping wing were reported by David et al (2012) and Tronchin et al. (2012), respectively, as illustrated in Figure 25.
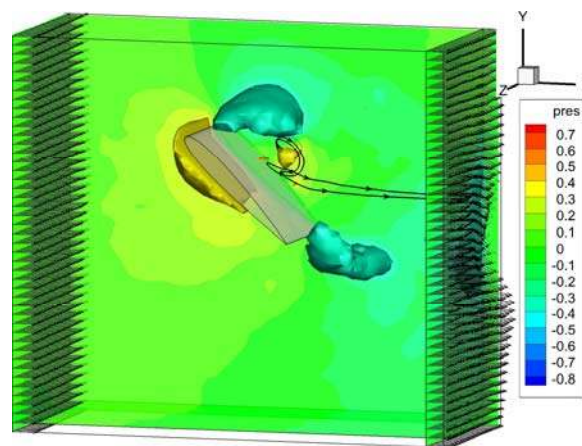

Figure 25. Sample pressure visualization of the instantaneous pressure field near the tip region of a flapping 3D wing (Tronchin et al. 2012).

Velocimetry-based pressure and loads determination has also been reported in a number of studies involving rotating wings or rotor geometries, usually based on phase-averaged measurement data. Berton et al (2004) applied phase-locked LDA to infer phase-resolved loads on helicopter rotor blades. Murai et al. (2007) used phase-locked PTV data to determine the pressure field of the 2D flow around a Savonius turbine rotor, some results from this study are given in Figure 26.
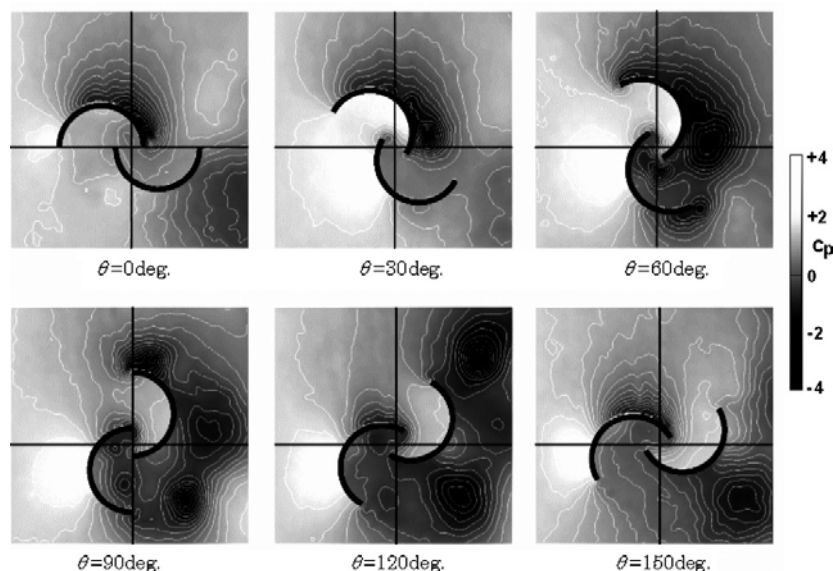
Figure 26. Pressure distributions around a Savonius rotor (Murai et al. 2007). Pressure distribution for various angles of attack at a tip speed ratio of 0.5.

In a number of subsequent publications, Ragni et al. (2011b, 2012ab) present the results of the non-intrusive PIV-based analysis of a propeller blade in a wind tunnel stream, determining both pressure fields and sectional forces, extending the measurement procedures used in the static airfoil study of Ragni et al. (2009). The stereo-PIV measurements are performed in phase-lock with the propeller rotation. The first study (Ragni et al. 2011b) considers the analysis of a single cross-section at 75% of the propeller radius, where the effect of spanwise flow is sufficiently low to justify a 2D analysis. The study compares the outcome when the analysis is made in either a stationary lab frame, in which the flow is unsteady as a result of the blade passage, or in a reference frame moving with the blade, with respect to which the flow can be assumed quasi-steady. The evaluation confirmed the equivalence of the two approaches. In a second study (Ragi et al. 2012a) the flow region near the tip was analysed by means of multiple, sequentially acquired planes to build a volumetric flow domain, in which the pressure and sectional-force distribution was determined. Finally in Ragni et al. (2012b) this approach was extended to quantify the flow around an entire propeller blade. Fourteen stereoscopic fields were acquired along the blade radius, that were merged into a three-dimensional volume extending over 85% of the entire blade span. Results for the velocity and pressure fields are depicted in Figure 27, including the extracted blade surface pressure distribution.
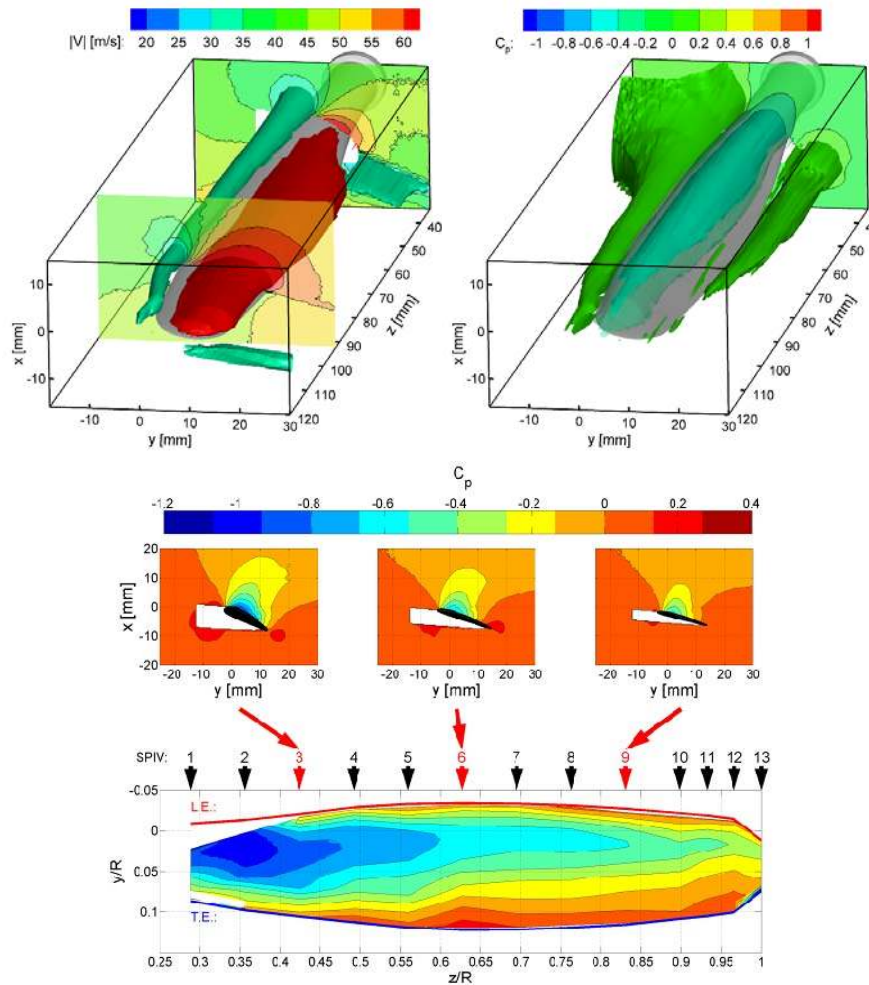
Figure 27.   Aerodynamic 3D analysis of an aircraft propeller blade based on multiple-plane, phase-locked stereo-PIV (Ragni et al. 2012b); volumetric visualization of absolute velocity (top left) and pressure coefficient (top right); blade surface pressure distribution (bottom).

As an example of pressure determination in the maritime regime, Di Felice et al. (2012) report on a PIV analysis of a naval propeller slipstream contraction. Stereoscopic PIV measurements were performed in phase-lock with the propeller rotation, at steps of 5 degrees for a characterization of the complete blade passage (i.e. 0-90 degrees). Additional planes with spacing of ±1 degree were obtained for the accurate determination of the radial and axial vorticity components. The pressure field was obtained from the volumetric distribution of the velocity gradient tensor that is the result of the phase-locked measurements, and computed using the Poisson formulation.

5.   Conclusions

A review has been given of principles and applications of employing PIV data as a basis for determining the fluid static pressure, by combining the measured velocity field with the flow governing equations. Especially the use of time-resolved PIV data offers a novel approach for instantaneous pressure determination. The added capabilities of three-dimensional PIV methods, such as tomographic PIV, further widen its potential as a non-intrusive diagnostic method for complex unsteady flows.

The operating principle of the method basically rests on the fact that, for incompressible flows, all kinematic terms in the momentum equation can be derived from (time-resolved) velocity field data, from which the pressure gradient can be readily computed. Usually the contribution of the viscous term can be neglected, leaving the material acceleration as the dominant term. The pressure can subsequently be computed, either from a direct spatial integration of the pressure gradient, or through a Poisson formulation. Several studies have been conducted that address and systematically assess the relevant parameters that influence the accuracy of the pressure determination, such as the propagation of the velocity error (noise), the influence of spatial and temporal resolution as well as the determination of the material acceleration from either a Eulerian or a Lagrangian perspective. Regarding the latter, the permitted time step of each method is limited by the associated time scale (convective for the Eulerian and intrinsic for the Lagrangian), which usually implies that for advection-dominated flow phenomena the Lagrangian approach provides a more accurate way of computing the material acceleration as it permits to increase the time step, which reduces the precision error.

Most studies applying PIV-based pressure determination have done so under the approximate assumption of 2D flow, often out of necessity in view of the essentially planar capability of PIV. The possible impact of omitting out-of-plane components have been revealed by recent studies in which a volumetric variant of PIV was used, and supported by experiment simulations. These show how a correct planar pressure extraction can be obtained with a thin-volume PIV variant, and simultaneously revealed that the planar approach with 2D data can be justified in case the out-of-plane components remain relatively small.

A discussion of a selection of applications, where PIV-based pressure determination has been used with success, may serve to illustrate the potentials provided by this new method and the possible impact it may have on future fluid-dynamic studies.

References

Abe S, Okamoto K, Madarame H (2004) The development of PIV-PSP hybrid system using pressure sensitive particles *Meas. Sci. Technol.* **15** 1153-1157

Adrian RJ (2005) Twenty years of particle image velocimetry *Exp. Fluids* **39** 159-169

Adrian RJ, Westerweel J (2011) *Particle Image Velocimetry*, Cambridge University Press

Albrecht T, Weier T, Gerbeth G, Metzkes H, Stiller J (2011) A method to estimate the planar, instantaneous body force distribution from velocity field measurements *Phys. Fluids* **23** 021702

Baur T, Köngeter J (1999) PIV with high temporal resolution for the determination of local pressure reductions from coherent turbulent phenomena *3rd Int. Workshop on PIV*, Santa Barbara, USA, 16-18 Sept. 1999, 101-106

Berton E, Maresca C, Favier D (2004) A new experimental method for determining local airloads on rotor blades in forward flight *Exp. Fluids* **37** 455-457

Boillot A, Prasad AK (1996) Optimization procedure for pulse separation in cross-correlation PIV *Exp. Fluids* **21** 87-93

Borowsky J, Wei T (2006) Simultaneous velocimetry/accelerometry measurements in a turbulent two-phase pipe flow *Exp. Fluids* **41** 13-20

Chang KA, Cowen EA, Liu PLF (1999) A multi-pulsed PTV technique for acceleration measurement *3rd Int. Workshop on PIV*, Santa Barbara, USA, 16-18 Sept. 1999, 451-456

Chang N, Ganesh H, Yakushiji R., Ceccio SL (2011) Tip vortex cavitation suppression by active mass injection *J. Fluids Eng.* **133** 111301

Charonko JJ, King CV, Smith BL, Vlachos PP (2010) Assessment of pressure field calculations from particle image velocimetry measurements *Meas. Sci. Technol.* **21** 105401

Christensen KT, Adrian RJ (2002) Measurement of instantaneous Eulerian acceleration fields by particle image velocimetry: method and accuracy *Exp. Fluids* **33** 759-769

David L, Jardin T, Farcy A (2009) On the non-intrusive evaluation of fluid forces with the momentum equation approach *Exp. Fluids* **52** 857-864

David L, Jardin T, Braud P, Farcy A (2012) Time-resolved scanning tomography PIV measurements around a flapping wing *Meas. Sci. Technol.* **20** 095401

DeGregorio F (2006) Aerodynamic performance degradation induced by ice accretion. PIV technique assessment in icing wind tunnel *13th Int. Symp. Apl. Laser Techn. to Fluid Mech.*, Lisbon, Portugal

DiFelice F, Felli M, Ragni D, Scarano F (2012) Investigation of vorticity and pressure distribution in a naval propeller slipstream contraction *Int. Workshop on the Application of PIV for Aeroacoustics and Noise*, Delft, The Netherlands, 16-17 April 2012, 67-73

Dong P, Hsu TY, Atsavaprenee P, Wei T (2001) Digital particle accelerometry *Exp Fluids* **30** 626-632

Elliot JA (1972) Microscale pressure fluctuations measured within the lower atmospheric boundary layer *J. Fluid Mech.* **53** 351-383

Elsinga GE, Scarano F, Wieneke B, Oudheusden van BW (2006) Tomographic particle image velocimetry *Exp. Fluids* **41** 933-947

Ferrari S, Rossi L (2008) Particle tracking velocimetry and accelerometry (PTVA) measurements applied to quasi-two-dimensional multi-scale flows *Exp. Fluids* **44** 873-886

Fujisawa N, Nakamura K, Srinivas K (2004) Interaction of two parallel plane jets of different velocities *J. Visualization* **7** 135-142

Fujisawa N, Tanahashi S, Srinvas K (2005) Evaluation of pressure field and fluid forces on a circular cylinder with and without rotational oscillation using velocity data from PIV measurement *Meas. Sci. Technol.* **16** 989-996

Fujisawa N, Nakamura K, Matsuura F, Sato Y (2006) Pressure field evaluation in microchannel junction flows through μPIV measurement *Microfluid Nanofluid* **2** 447-453

Fujisawa N, Oguma Y (2008) Measurement of pressure field around a NACA0018 airfoil from PIV velocity data *J. Visualization* **4** 281-282

Ghaemi S, Ragni D, Scarano F (2012) PIV-based evaluation of pressure fluctuations within the turbulent boundary layer *16th Int. Symp. on Applications of Laser Techniques to Fluids Mechanics,* Lisbon, Portugal, 9-12 July 2012 (*Exp. Fluids*, in press)

Gharali K, Johnson DA (2008) Pressure and acceleration determination methods using PIV velocity data *FEDSM2008-55157* 2008 ASME Fluids Engineering Conference, 10-14 Aug 2008, Jacksonville, USA

Gurka R, Liberzon A, Hefetz D, Rubinstein D, Shavit U (1999) Computation of Pressure Distribution Using PIV Velocity Data *3rd Int. Workshop on PIV*, Santa Barbara, USA, 16-18 Sept. 1999, 671-676

Haigermoser C (2009) Application of an acoustic analogy to PIV data from rectangular cavity flows *Exp. Fluids* **47** 145-157

Henning A, Kaepernick K, Ehrenfried K, Koop L, Dillmann A (2008) Investigation of aeroacoustic noise generation by simultaneous particle image velocimetry and microphone measurements *Exp. Fluids* **45** 1073-1085

Hong YS, Altman A (2208) Lift from spanwise flow in simple flapping wings *J. Aircraft* **45** 1206-1216

Hosokawa S, Moriyama S, Tomiyama A, Takada N (2003) PIV measurement of pressure distributions about single bubbles *J. Nuclear Sci. Technol.* **40** 754-762

Imaichi K, Ohmi K (1983) Numerical processing of flow-visualization pictures – measurement of two-dimensional flow *J. Fluid Mech. 129* 283-311

Jakobsen ML, Dewhirst TP, Greated CA (1997) Particle Image Velocimetry for predictions of acceleration fields and forces within fluid flows *Meas. Sci. Techn.* **8** 1502-1516

Jardin T, Chatellier L, Farcy A, David L (2009) Correlation between vortex structures and unsteady loads for flapping motion in hover *Exp. Fluids* **47** 655-664

Jardin T, David L, Farcy A (2009) Characterization of vortical structures and loads based on time-resolved PIV for asymmetric hovering flapping flight *Exp. Fluids* **46** 847-857

Jaw SY, Chen JH, Wu PC (2009) Measurement of pressure distribution from PIV experiments *J. Visualization* **12** 27-35

Jensen A, Pedersen GK, Wood DJ (2003) An experimental study of wave run-up at a steep beach *J. Fluid Mech.* **486** 161-188

Jensen A, Pedersen GK (2004) Optimization of acceleration measurements using PIV *Meas. Sci. Technol.* **15** 2275-2283

Jensen A, Sveen JK, Grue J, Richon JB, Gray C (2001) Accelerations in water waves by extended particle image velocimetry *Exp. Fluids* **30** 500-510

Joshi P, Liu X, Katz J (2012) Modification of turbulence in boundary layers by mean and fluctuating pressure gradients, FEDSM2012-72280, ASME 2012 Fluids Engineering Summer Meeting, 8-12 July 2012, Puerto Rico, USA.

Kähler CJ, Kompenhans J (2000) Fundamentals of multiple plane stereo PIV *Exp. Fluids* **29** S70–S77

Kat de R, Oudheusden van BW, Scarano F (2008) Instantaneous planar pressure field determination around a square-section cylinder based on time-resolved stereo-PIV *14th Int. Symp. on Applications of Laser Techniques to Fluids Mechanics*, Lisbon, Portugal, 7-10 July 2008, paper 1259

Kat de R, Oudheusden van BW, Scarano F (2009) Instantaneous pressure field determination in a 3D flow using time-resolved thin volume tomographic-PIV *8th Int. Symp. on PIV*, Melbourne, Australia, 25-28 Aug. 2009

Kat de R, Oudheusden van BW (2010a) Instantaneous planar pressure from PIV: analytic and experimental test-cases *15th Int Symp on Applications of Laser Techniques to Fluids Mechanics*, Lisbon, Portugal, 5-8 July 2010

Kat de R, Humble RA, Oudheusden van BW (2010b) Time-resolved PIV study of a transitional shear-layer around a square-section cylinder *IUTAM Symposium on Bluff Body Wakes and Vortex Induced Vibrations BBVIV-6* Capri, Italy, 22-25 June 2010

Kat de R, Oudheusden van BW (2012) Instantaneous planar pressure determination from PIV in turbulent flow *Exp. Fluids* **52** 1089-1106

Kat R de (2012) Instantaneous planar pressure determination from particle image velocimetry *PhD Thesis* Delft University of Technology, ISBN 978-90-818719-0-7

Kat R de, Ganapathisubramani B (2012) Pressure from particle image velocimetry for convective flows: A Taylor's hypothesis approach *Meas. Sci. Technol.* (in press)

Khodarahmi I, Shakeri M, Sharp MK, Amini AA (2010) Using PIV to determine relative pressures in a stenotic phantom under steady flow based on the pressure-Poisson equation *Proc. 32nd Annual International Conference of the IEEE EMBS*, Buenos Aires, Argentina, 31 Aug - 4 Sept 2010, 2594-2597

Kimura F, Khalil G, Zettsu N, Xia Y, Callis J, Gouterman M, Dalton L, Dabiri D, Rodriguez M (2006) Dual luminophore microspheres for pressure-sensitive luminescent imaging *Meas Sci. Technol.* **17** 1254-1260

Kimura F, McCann J, Khalil G, Dabiri D Xia Y, Callis JB (2010) Simultaneous velocity and pressure measurement using luminescent microspheres *Rev. Sci.Instr..* **81** 064101

Klein C, Engler RH, Henne U, Sachs WE (2005) Application of pressure-sensitive paint for determination of the pressure field and calculation of the forces and moments of models in a wind tunnel *Exp. Fluids* **39** 475-483

Koschatzky V, Moore PD, Westerweel J, Scarano F, Boersma BJ (2011a) High speed PIV applied to aerodynamic noise investigation *Exp. Fluids* **50** 863-876

Koschatzky V, Westerweel J, Boersma BJ (2011b) A study on the application of two different acoustic analogies to experimental PIV data *Phys.Fluids* **23** 065112

Koschatzky V, Overmars EFJ, Boersma BJ, Westerweel J (2012) Comparison of planar PIV and tomographic PIV for aeroacoustics *16th Int. Symp. on Applications of Laser Techniques to Fluids Mechanics,* Lisbon, Portugal, 9-12 July 2012

Kotsonis M, Ghaemi S, Veldhuis L, Scarano F (2011) Measurement of the body force field of plasma actuators *J. Phys. D: Appl. Phys.* **44** 045204

Kunze S, Brücker C (2011) Flow control over an undulating membrane *Exp. Fluids* **50** 747-759

Kurtulus DF, Scarano F, David L (2007) Unsteady aerodynamic forces estimation on a square cylinder by TR-PIV *Exp. Fluids* **42** 185-196

LaPorta A, Voth GA, Crawford AM, Alexander J, Bodenschatz E (2001) Fluid particle accelerations in fully developed turbulence *Nature* **409** 1017-1019

Lemke M, Sesterhenn J (2012) Instantaneous pressure determination in compressible flows from PIV-data by an adjoint based data assimilation *Int. Workshop on the Application of PIV for Aeroacoustics and Noise*, Delft, The Netherlands, 16-17 April 2012, 85-88

Liu X, Katz J (2004) Measurement of pressure distribution in a cavity flow by integrating the material acceleration *HT-FED2004-56373 2004 ASME Heat Transfer/Fluids Engineering Summer Conference*, Charlotte, USA, 11-15 July 2004

Liu X, Katz J (2006) Instantaneous pressure and material acceleration measurements using a four-exposure PIV system *Exp. Fluids* **41** 227-240

Liu X, Katz J (2007) A comparison of cavitation inception index measurements to the spatial pressure distribution within a 2D cavity shear flow *FEDSM2007-37090, 2007 ASME Fluids Engineering Conference*, San Diego, USA, 30 July - 2 Aug 2007

Liu X, Katz J (2008) Cavitation phenomena occurring due to interaction of shear layer vortices with the trailing corner of a two-dimensional open cavity *Phys. Fluids* **20** 041702

Liu X, Katz J (2011) Time resolved measurement of the pressure field generated by vortex-corner interactions in a cavity shear layer *AJK2011-08018, ASME-JSME-KSME Joint Fluids Engineering Conference*, Hamamatsu, Japan, 24-29 July 2011

Lorenzoni V, Moore P, Scarano F, Tuinstra M (2009) Aeroacoustic analysis of a rod-airfoil flow by means of time-resolved PIV *AIAA 2009-3298, 15th AIAA/CEAS Aeroacoustics Conference (30th AIAA Aeroacoustics Conference)*, Miami, USA, 11-13 May 2009

Lorenzoni V, Moore P, Scarano F (2010) Characterization of noise sources in a rod-airfoil configuration by means of time-resolved tomographic PIV *AIAA 2010-3898, 16th AIAA/CEAS Aeroacoustics Conference (31st AIAA Aeroacoustics Conference)*, Stockholm, 7-9 June 2010

Lorenzoni V, Tuinstra M, Scarano F (2012) On the use of time-resolved particle image velocimetry for the investigation of rod-airfoil acoustics *J. Sound Vibr.* **331** 5012-5027

McLachlan BG, Kavandi JL, Callis JB, Gouterman M, Green E, Khalil G, Burns D (1993) Surface pressure field mapping using luminescent coatings *Exp. Fluids* **14** 33-41

Moore P, Lorenzoni, Scarano F (2011) Two techniques for PIV-based aeroacoustic prediction and their application to a rod-airfoil experiment *Exp Fluids* **50** 877-855

Murai Y, Nakada T, Suzuki T, Yamamoto F (2007) Particle tracking velocimetry applied to estimate the pressure field around a Savonius turbine *Meas. Sci. Technol.* **18** 2491-2503

Murray N, Ukeiley L, Raspet R (2007) Calculating surface pressure fluctuations from PIV data using Poisson's equation *AIAA-2007-1306, 45th AIAA Aerospace Science Meeting,* Reno, USA, 8-11 Jan. 2007

Noca F, Shiels D, Jeon D (1999) A comparison of methods for evaluating time-dependent fluid dynamic forces on bodies, using only velocity fields and their derivatives *J. Fluids Struct.* **13** 551-578

Novara M, Scarano F (2012) Lagrangian acceleration evaluation for tomographic PIV: a particle tracking based approach *16th Int. Symp. on Applications of Laser Techniques to Fluids Mechanics,* Lisbon, Portugal, 9-12 July 2012

Okuno T, Sugii Y, Nishio S (2000) Image measurement of flow field using physics-based dynamic model *Meas. Sci. Technol.* **11** 667-676

Ooi KK, Acosta AJ (1983) The utilization of specially tailored air bubbles as static pressure sensors in a jet *J. Fluids Eng.* **106** 459-465

Oudheusden van BW, Scarano F, Casimiri EWF (2006) Non-intrusive load characterization of an airfoil using PIV *Exp. Fluids* **40** 988-992

Oudheusden van BW, Scarano F, Roosenboom EWM, Casimiri EWF, Souverein LJ (2007) Evaluation of integral forces and pressure fields from planar velocimetry data for incompressible and compressible flows *Exp. Fluids* **42** 153-162

Oudheusden van BW, Souverein LJ (2007) Principles and application of velocimetry-based planar pressure imaging in compressible flows with shocks *7th Int. Symp. on PIV*, Rome, Italy, 11-14 Sept 2007

Oudheusden van BW (2008) Principles and application of velocimetry-based planar pressure imaging in compressible flows with shocks *Exp. Fluids* **45** 657-674

Perret L, Braud P, Fourment C, David L, Delville J (2006) 3-Component acceleration field measurement by dual-time stereoscopic particle image velocimetry *Exp. Fluids* **40** 813-824

Pröbsting S, Scarano F, Bernardini M, Pirozzoli S (2012) A comparative study of turbulent boundary layer wall pressure fluctuations obtained from high-speed tomographic PIV and DNS *16th Int. Symp. on Applications of Laser Techniques to Fluids Mechanics,* Lisbon, Portugal, 9-12 July 2012

Raffel M, Willert CE, Wereley ST, Kompenhans, (2007) *Particle Image Velocimetry. A Practical Guide*, 2nd ed., Springer, Berlin

Ragni D, Ashok A, Oudheusden van BW, Scarano F (2009) Surface pressure and aerodynamic loads determination of a transonic airfoil based on particle image velocimetry *Meas. Sci. Technol.* **20** 074005

Ragni D, Oudheusden van BW, Scarano F (2011a) Drag coefficient accuracy improvement by means of particle image velocimetry for a transonic NACA0012 airfoil *Meas. Sci. Technol.* **22** 017003

Ragni D, Oudheusden van BW, Scarano F (2011b) Non-intrusive aerodynamic loads analysis of an aircraft propeller blade *Exp. Fluids* **51** 361-371

Ragni D, Oudheusden van BW, Scarano F (2012a) 3D pressure imaging of a propeller blade tip region by phase-locked stereoscopic PIV *Exp. Fluids* **52** 463-477

Ragni D, Oudheusden van BW, Scarano F (2012b) PIV-load determination in aircraft propellers *16th Int. Symp. on Applications of Laser Techniques to Fluids Mechanics,* Lisbon, Portugal, 9-12 July 2012

Ran B, Katz J (1994) Pressure fluctuations and their effect on cavitation inception within water jets *J Fluid Mech* **262** 223-263

Regert T, Chatellier L, Tremblais B, David L (2011) Determination of pressure fields from time-resolved data *9th Int Symp on PIV ,* Kobe, Japan, 21-23 July 2011

Rival D, Manejev E, Tropea C (2010a) Measurement of parallel blade-vortex interaction at low Reynolds numbers *Exp. Fluids* **49** 89-99

Rival D, Schönweitz D, Tropea C (2010b) Vortex interaction of tandem pitching and plunging plates: a two-dimensional model of hovering dragonfly-like flight *Bioinsp. Biomim.* **6** 016008

Ruhnau P, Schnorr (2007) Optical Stokes flow estimation: an imaging-based control approach *Exp. Fluids* **42** 61-78

Scarano F (2013) Tomographic PIV: principles and practice *Meas. Sci. Technol.*

Schwabe M (1935) Über die Druckermittlung in der nichtstationären ebenen Strömung *Ing. Archiv* **6** 34-50

Schram C, Hirschberg A, Verzicco R (2004) Sound produced by vortex pairing: prediction based on Particle Image Velocimetry. *AIAA J.* **42** 2234-2244

Schröder A, Herr M, Lauke T, Dierksheide U (2006) A study on trailing-edge noise sources using high-speed particle image velocimetry *Notes on Numerical Fluid Mechanics* **92** 373-380

Sjörs K, Samuelsson I (2005) Determination of the total pressure in the wake of an airfoil from PIV data *PIVNET II International Workshop on the Application of PIV in Compressible Flows*, Delft, The Netherlands, paper 14

Souverein LJ, Oudheusden van BW, Scarano F (2007) Particle image velocimetry based loads determination in supersonic flows *AIAA-2007-0050*, 45th AIAA Aerospace Science Meeting, 8-11 Jan 2007, Reno, USA.

Spedding GR, Hedenström A (2009) PIV-based investigations of animal flight *Exp. Fluids* **46** 749-763

Sridhar and Katz (1995) Drag and lift forces on microscopic bubbles entrained by a vortex *Phys. Fluids* **7** 389-399

Suryadi A, Obi S (2011) The estimation of pressure on the surface of a flapping rigid plate by stereo PIV *Exp. Fluids* **51** 1403-1416

Tronchin T, Farcy A, David L (2012) Evaluation of pressure field and fluid forces for 3D flow around flapping wing *Int. Workshop on the Application of PIV for Aeroacoustics and Noise*, Delft, The Netherlands, 16-17 April 2012, 59-62

Tsuji Y, Fransson JHM, Alfredsson PH, Johansson AV (2007) Pressure statistics and their scaling in high-Reynolds-number turbulent boundary layers *J. Fluid Mech.* **585** 1-40

Uda T, Nishikawa A, Someya S, Iida A (2011) Prediction of aeroacoustic sound using the flow field obtained by time-resolved particle image velocimetry *Meas. Sci. Technol.* **22** 075402

Unal MF, Lin JC, Rockwell D (1997) Force prediction by PIV imaging: a momentum based approach *J. Fluids Struct.* **11** 965-971

Vanierschot M, Bulck van den E (2008) Planar pressure field determination in the initial merging zone of an annular swirling jet based on stereo-PIV measurements *Sensors* **8** 7596-7608

Violato D, Bryon K, Moore P, Scarano F (2010) Application of Powell's analogy for the prediction of vortex-pairing sound in a low-Mach number jet based on time-resolved planar and tomographic PIV *AIAA 2010-3959, 16th AIAA/CEAS Aeroacoustics Conference (31st AIAA Aeroacoustics Conference*, Stockholm, 7-9 June 2010

Violato D, Moore P, Scarano F (2011) Lagrangian and Eulerian pressure field evaluation of rod-airfoil flow from time-resolved tomographic PIV *Exp. Fluids* **50** 1057-1070

Voth GA, Satyanarayan K, Bodenschatz E (1998) Lagrangian acceleration measurements at large Reynolds numbers *Phys Fluids* **10** 2268-2280

Virant M, Dracos T (1997) 3D PTV and its application on Lagrangian motion *Meas. Sci. Technol.* **8** 1539-1552

Willert CE, Gharib M (1991) Digital particle image velocimetry *Exp. Fluids* **10** 181-193